Probing the internal structure of the asteriod Didymoon with a passive seismic investigation

Naomi Murdoch, Stefanie Hempel, Sophal Laurent Pou, Alexandre Cadu, Raphaël Garcia, David Mimoun, Ludovic Margerin, Ozgur Karatekin

Probing the internal structure of the asteriod Didymoon with a passive seismic investigation

N. Murdoch [a,*], S. Hempel [a], L. Pou [a], A. Cadu [a], R.F. Garcia [a], D. Mimoun [a], L. Margerin [b], O. Karatekin [c]

[a] Institut Supérieur de l'Aéronautique et de l'Espace (ISAE-SUPAERO), Université de Toulouse, 31400 Toulouse, France
[b] IRAP-CNRS, Université Toulouse 3, 31400 Toulouse, France
[c] Royal Observatory of Belgium, Brussels, Belgium

Keywords:
Asteroid
Geophysics
Tidal forces
Seismology

A B S T R A C T

Understanding the internal structure of an asteroid has important implications for interpreting its evolutionary history, for understanding its continuing geological evolution, and also for asteroid deflection and in-situ space resource utilisation. Given the strong evidence that asteroids are seismically active, an in-situ passive seismic experiment could provide information about the asteroid surface and interior properties. Here, we discuss the natural seismic activity that may be present on Didymoon, the secondary component of asteroid (65803) Didymos. Our analysis of the tidal stresses in Didymoon shows that tidal quakes are likely to occur if the secondary has an eccentric orbit. Failure occurs most easily at the asteroid poles and close to the surface for both homogeneous and layered internal structures.

Simulations of seismic wave propagation in Didymoon show that the seismic moment of even small meteoroid impacts can generate clearly observable body and surface waves if the asteroid's internal structure is homogeneous. The presence of a regolith layer over a consolidated core can result in the seismic energy becoming trapped in the regolith due to the strong impedance contrast at the regolith-core boundary. The inclusion of macroporosity (voids) further complexifies the wavefield due to increased scattering. The most prominent seismic waves are always found to be those traveling along the surface of the asteroid and those focusing in the antipodal point of the seismic source. We find also that the waveforms and ground acceleration spectra allow discrimination between the different internal structure models.

Although the science return of a passive seismic experiment would be enhanced by having multiple seismic stations, one single seismic station can already vastly improve our knowledge about the seismic environment and sub-surface structure of an asteroid. We describe several seismic measurement techniques that could be applied in order to study the asteroid internal structure with one three-component seismic station.

1. Introduction

The internal structure of an asteroid has important implications for interpreting its evolutionary history (we may expect to find huge voids inside an asteroid that was formed from collisional disruption and reaccumulation of major fragments; Michel et al., 2001) and also for understanding its continuing geological evolution (a microporous body may compact due to pore crushing during an impact whereas the voids in a macroporous rubble pile may protect the body causing more localized and less extensive damage; Jutzi et al., 2008). Such knowledge can also inform us about the collisional processes responsible for planetary formation and hence improve our understanding of the formation and evolution of the entire Solar System. Knowledge about the internal structure of asteroids also has, of course, strong implications for possible asteroid mitigation and deflection techniques (e.g., Cheng et al., 2016), and for in-situ space resource utilisation (Graps et al., 2016).

Bulk asteroid properties determined from remote observations and in-situ observations from space missions can help to constrain the physical properties and internal structure of asteroids. For example, spin rates can inform us about the overall strength of an asteroid; small, fast-rotating bodies must possess some cohesive strength (Holsapple, 2007a). Reflectance spectra or albedo measurements can provide an asteroid's surface composition allowing analogue meteorites to be identified (DeMeo et al., 2015). A comparison of the bulk density of the asteroid

* Corresponding author.
E-mail address: naomi.murdoch@isae.fr (N. Murdoch).

http://dx.doi.org/10.1016/j.pss.2017.05.005

with the analogue meteorite's grain density can indicate that there is a significant amount of porosity (or of high density material) within the asteroid (e.g., Britt and Consolmagno, 2000; Consolmagno et al., 2008; Carry, 2012). However, determining an asteroid's density requires both a mass estimate (there are currently only a small number of asteroids with mass determinations) and a volume estimate (there are inherently large uncertainties from remote observations; Carry, 2012).

Interpreting the morphology and surface features that are visible in close-up images obtained during recent space missions can help to further constrain the physical properties of the surface and sub-surface. Some examples are the impressive faults observed on Vesta that may indicate a differentiated internal structure (Buczkowski et al., 2012), or the strange shapes of asteroids Eros and Gaspra that indicate that these bodies have some internal strength. Even crater morphology and ejecta can give information about the asteroid mechanical properties (Housen and Holsapple, 2003; Asphaug, 2008). However, until we perform direct geophysical exploration of asteroids, all inferences about asteroid interiors from observations and space missions are purely educated guesses.

At the beginning of planetary exploration, surface-based geophysics was considered a key technique for understanding a planetary body and its interior: the first instruments sent to the surface of another planetary body were seismometers (Rangers 3–5; sent to the Moon in 1962), the first landers sent to Mars carried seismometers (Viking Landers 1 and 2; 1975–1977), and the Venera 13 and 14 Venus landers (1981) also contained seismic instruments. However, despite several mission studies and proposals over the years e.g., (Gonzalez et al., 2004; Robert et al., 2010), a seismic investigation has never previously been performed on an asteroid.

There is, nonetheless, strong evidence that asteroids are seismically active; factors such as crater erasure (Thomas and Robinson, 2005), destabilisation of regolith slopes (Richardson et al., 2005), and regolith segregation (Miyamoto et al., 2007) provide evidence for impact-induced seismic shaking of small bodies. Seismic signals may also occur from alternative natural sources such as thermal cracks (Delbo et al., 2014), internal quakes due to tidal forces (Richardson et al., 1998a) and other geophysical processes see (Murdoch et al., 2015). Here we discuss the possibility of performing a passive seismic experiment on Didymoon; the secondary component of asteroid (65803) Didymos and the target of the joint ESA-NASA mission AIDA (Cheng et al., 2016; Michel et al., 2016). Such an in-situ geophysical investigation could provide information about the surface and interior properties of Didymoon, shedding light on mechanisms involved in binary asteroid formation and the subsequent geophysical evolution of the asteroid's surface and interior. While such an investigation may be focussed on only one asteroid, its scientific implications would reach across our Solar System and beyond, providing knowledge about the fundamental processes of planetary formation and small body evolution.

In this paper we first outline the evidence for asteroid seismicity (Section 2). In Section 3, we present the physical and dynamical assumptions made in this paper about the Didymos binary asteroid system including the various internal structure models considered. Then, we discuss in more detail the natural seismic sources that may be active on and inside Didymoon (Section 4) before presenting a detailed analysis of the tidal stresses in Didymoon (Section 5). In Section 6 we simulate the seismic wavefields that may propagate in Didymoon, before finishing with a discussion about how we will be able to determine the internal structure of Didymoon using seismic measurements (Section 7).

2. Evidence for asteroid seismicity

Meteoroid impacts onto an asteroid can generate significant seismic shaking e.g., (Asphaug et al., 1996a; Garcia et al., 2015). Such shaking may cause a net downslope movement of loose surface material (Richardson et al., 2005). The first direct evidence for such seismic shaking on an asteroid was presented by Thomas and Robinson (2005). They showed that the formation of a relatively young crater on asteroid Eros resulted in the removal of other craters as large as 0.5 km over nearly 40% of the asteroid's surface. As burial by ejecta cannot explain the observed pattern of crater removal, and the areas with a lower than expected number of small craters correlate well with radial distance from the Shoemaker crater, they conclude that seismic shaking is the most probable mechanism.

A deficiency of craters (compared to predictions of dynamical models of projectile populations) has been seen on many asteroids surfaces; Itokawa has very few craters in general and absolutely no distinct craters <1 m in diameter (Saito et al., 2006; Fujiwara et al., 2006), Eros and Lutetia have a deficiency of small (<1–2 km diameter) craters (Veverka et al., 2000, 2001; Sierks et al., 2011), and on Vesta there is evidence of smoothing and erasure of small features well beyond the extent of the ejecta blankets of the large impacts (Vincent et al., 2013). In addition to complete crater erasure, the filled-in interiors and subdued rims of several craters (Veverka et al., 2001; Robinson et al., 2002; Zuber et al., 2000) indicate that there are active crater degradation processes occurring on asteroids. In fact, more generally, all asteroids that have been visited by space missions have shown diverse evidence for regolith motion. Bright surface features can be seen in regions that have steep slopes, areas of local high terrain and apparently eroded areas, e.g., crater rims, while dark soils are typically located at the bases of bright streaks and display both diffuse and sharp boundaries e.g., (Veverka et al., 2000; Thomas et al., 2002; Riner et al., 2008; Jaumann et al., 2012). The bright streaks imply freshly exposed material that has not yet been subjected to space weathering thus indicating that regolith has been relocated since the initial accumulation or deposition (Saito et al., 2006). These observations, combined with morphological data, suggest that there are often preferential downslope movements or landslides of mature regolith that reveal immature material beneath e.g., (Robinson et al., 2002; Thomas et al., 2002; Riner et al., 2008; Murchie et al., 2002; Williams et al., 2013; Yingst et al., 2014). On Itokawa, further evidence for landslide-like deposits are the large boulders that have blocked the migration of smaller particles, resulting in piles of smaller particles on the uphill sides of the boulders Fig. 1b; Miyamoto et al., 2007). Additionally, the positions and orientations of the particles at the boundary of the Muses Sea region with the rough terrain indicate that they are stable against local gravity and that the migrations were gravity-induced (Miyamoto et al., 2007). Although alternative processes have been suggested including microcratering and thermal creep; (Cheng, 2002), impact-induced seismic shaking is considered as the most likely mechanism behind both crater erasure and regolith motion on asteroid surfaces e.g., (Richardson et al., 2004; Michel et al., 2009). However, the necessity of a triggering mechanism to provoke downslope regolith motion is currently under debate (Holsapple, 2013). Seismic shaking may also be responsible for the observed regolith size segregation (Asphaug et al., 2001; Miyamoto et al., 2007; Murdoch et al., 2015).

Numerous tectonic features have been documented on asteroids i.e., surface features created by internal stresses that fracture or deform the surface layer (Murdoch et al., 2015). However, tectonic deformation cannot occur without forces to drive it. One such force is the impact-induced compression that is thought to have produced the large “spiral” pattern on Eros (Watters et al., 2011; Cheng et al., 2002; Veverka et al., 2000), the lineaments on Lutetia (Besse et al., 2014) and the large equatorial and northern troughs on Vesta's surface (Jaumann et al., 2012). Other possible sources of tectonic stress include changes in rotation rate due to the effect of solar radiation known as the YORP effect, which may cause tectonic arrangements or landslide-like surface modifications towards the equator (Harris et al., 2009; Walsh et al., 2008) and thermal stresses (Dombard and Freed, 2002).

3. The Didymos binary asteroid properties

Didymos is characterised as an S-type object (de Leon et al., 2010). Following the ESA AIM Didymos Reference Model (AIM-A Team, 2015),

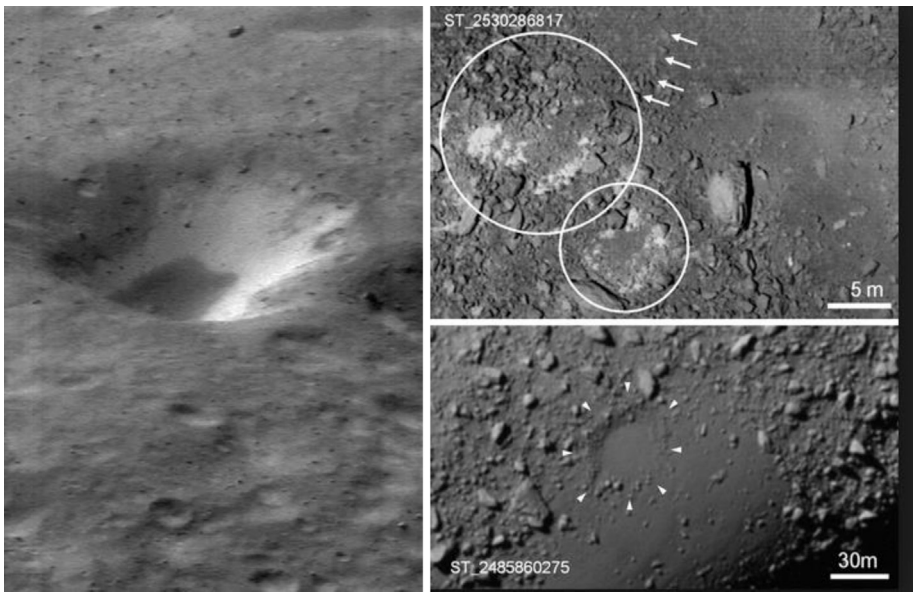

Fig. 1. Evidence of regolith motion on asteroids - LEFT: Bright, freshly exposed material on a large crater wall, as the darker material moves downslope (NEAR image PIA03134; Credit NASA/JPL/JHUAPL); TOP RIGHT: Image of the Neck area of Itokawa (13 cm/pixel) showing piles of angular boulders at the lower part of the image. Crater-like depressions are shown by the circles and the arrows indicate the debris, which appears to have drained from the rim of the upper crater towards the smooth terrain; BOTTOM RIGHT: A circular depression that appears to be filled with finer particles. Figures from Murdoch et al. (2015).

we assume that Didymain (the primary) and Didymoon (the secondary) both have a bulk density of 2146 kg/m^3, with an uncertainty of 30% (Scheirich and Pravec, 2009). The mean diameter of Didymain is 775 m, and the mean distance between the center of the primary and the center of the secondary is 1180 m (Scheirich and Pravec, 2009). Didymoon has a mean diameter of 163 m and a likely retrograde orbit around Didymain with a rotation period of 11.9 h and an eccentricity of, at most, 0.03 (Scheirich and Pravec, 2009). Although Didymoon is too small to be resolved from the Earth, it has been predicted that Didymoon is spin-locked and that it has an ellipsoidal shape with the nominal values of the semi-axes being $a = 103$ m, $b = 79$ m and $c = 66$ m (AIM-A Team, 2015).

In this paper we consider four different internal structure models for Didymoon. Given the large uncertainties in the form and internal structure of Didymoon, we start with the most simple model possible; a spherical consolidated body with constant density (Fig. 2 a). Then we consider two internal structure models consisting of a spherical homogeneous consolidated body covered with regolith layers of a globally constant thickness of 1 m and 10 m, respectively (Figs. 2 b, c). As we have not yet visited a binary asteroid, and we have no thermal inertia measurements of Didymoon, the regolith properties are entirely unknown. We, therefore, assume that the regolith properties are equal to lunar mega-regolith properties (Cooper et al., 1974; Horvath et al., 1980; Gagnepain-Beyneix et al., 2006; Garcia et al., 2015).

In order to discuss seismic waveforms and travel-times as a function of regolith depth only, we introduce a set of models that are mass-inconsistent, but for which the physical properties of the regolith layer and the asteroid core stay constant (Fig. 3). Consequent mass-deficits amount to 1 and 10%, respectively. The impedance contrasts at the regolith-core boundary amount to a 30% variation in P-wave velocity and a 20% variation in S-wave velocity.

Given that S-type asteroids are known to have macro-porosity (Scheeres et al., 2015), we have also investigated a macro-porous internal structure model by including voids (Fig. 2 d). The voids are distributed uniformly throughout the asteroid both in depth and latitude. Their size follows a Gaussian distribution with an average diameter of 5 m and standard deviation of 1.5 m, allowing overlap of voids, giving an overall macro-porosity of ~7%.

In all of the internal structure models, seismic velocities are computed from the assumed bulk density (ρ in g/cm^3) using Gardner's relation $V_p = (\rho/\alpha)^{(1/\beta)}$, and $V_s = V_p(1-2\nu)/2(1-\nu)$ using $\alpha = 0.31$, $\beta = 0.25$ and a Poisson ratio of $\nu = 0.25$ (Gardner et al., 1974). Fig. 3 shows the density profiles for the internal structure models without voids. Concerning the seismic attenuation, quality factors (inversely proportional to attenuation) as high or higher than on the Moon, i.e. $Q \geq 1000$ see e.g. (Gillet et al., 2017) may be observed in asteroids. However, recent impact experiments into a loose regolith layer suggest a low quality factor at high frequencies (Kedar et al., 2012). As the influence of varying the frequency-independent seismic attenuation (quality factors, $Q = 20, 100, 1000$) has previously been investigated by Garcia et al. (2015), in this

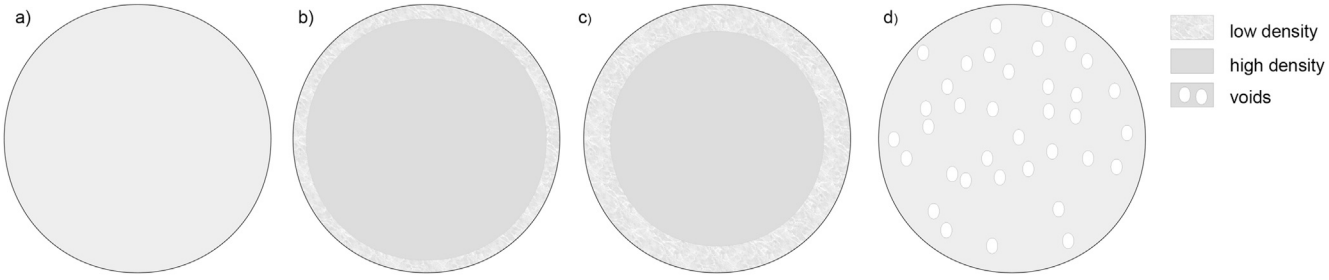

Fig. 2. Schematics of the Didymoon internal structure models - We consider four cases: (a) a consolidated body with constant density and seismic velocities, (b) and (c) a layered body consisting of a homogeneous consolidated body covered with a regolith layer of a globally constant thickness of 1 m and 10 m, respectively, and d) a macro-porous internal structure model including voids extending to the deep interior. The schematics are not to scale. See Fig. 3 for the density profiles for the internal structure models without voids.

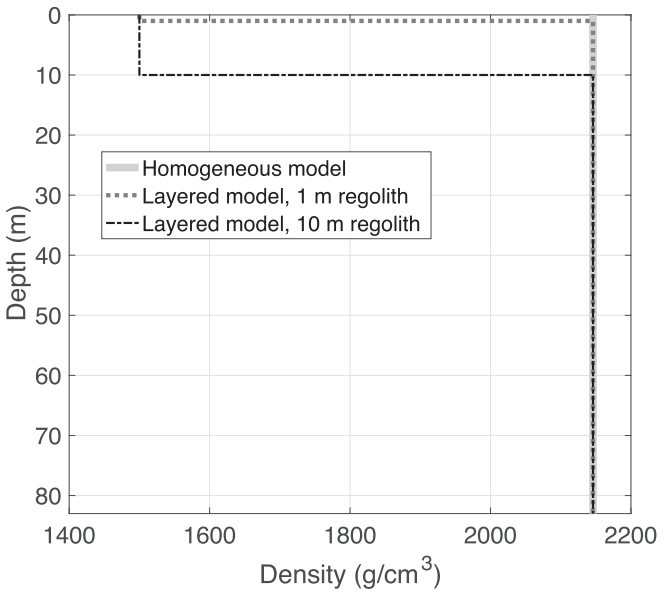

Fig. 3. Density profiles assumed for a homogeneous Didymoon (Fig. 2 a), as well as for the layered internal structure model (Fig. 2 b and c) with regolith thicknesses of 1 m and 10 m. The core density is 2146 g/cm^3, with a corresponding P-wave seismic velocity of 2297 m/s.

paper we assume the very conservative value of $Q = 100$ for the seismic attenuation. We do not include a frequency-dependent quality factor, as the frequency dependence is poorly constrained. Also poorly constrained is the ratio between P-wave attenuation and S-wave attenuation Q_P/Q_S, for which reason we assume a ratio of 1.

4. Natural seismic sources at Didymoon

4.1. Meteoroid impacts

Meteoroids are small particles in space, usually orbiting the Sun. The seismic source created by meteoroid impacts has been studied both by numerical methods (Walker and Huebner, 2004) and by experiments (Kedar et al., 2012; Yasui et al., 2015). The seismic moment tensor for an impact is usually assumed to be similar to that of an explosion (Walker and Huebner, 2004). Various scaling relations relating impactor and target parameters to seismic moment have been provided such as:

$$M_0 = \left(\frac{\varepsilon E_k}{4.8e-9}\right)^{(1/1.24)} \quad (1)$$

where $E_k = \frac{1}{2}mv^2$ is the kinetic energy (in Joules) of an impactor of mass m and velocity v, M_0 is the seismic moment of interest here (in N.m), and ε is the seismic efficiency, which is the ratio between the seismic energy and the impact kinetic energy. Equation (1) is provided by Teanby and Wookey (2011) and depends on the seismic efficiency which is usually poorly known. This parameter ranges from 10^{-6} to 10^{-2} in the literature see discussion in Garcia et al. (2015). However, the seismic efficiency is generally predicted to be larger for low energy impacts than for high energy impacts (Edwards et al., 2008). Using this relation, a 10 g and 1 mg meteoroid impacting a homogeneous Didymoon with density 2146 kg/m^3 at 6 km/s produce explosive seismic moments of 8.2e+06 N.m and 4.9e+03 N.m, respectively.

An estimation of the likely meteoroid impact frequency F (in year^{-1}) for Didymoon can be calculated as follows (O'Brien et al., 2011): $F = P_{IC}\left(\frac{D_T+D_I}{2}\right)^2 N$, where P_{IC} is the intrinsic collision probability (estimated to be $\sim 15 \times 10^{18}$ km^{-2} yr^{-1} for Near Earth Asteroids (NEAs) hitting other NEAs; Bottke et al., 1994), D_T and D_I are the diameters (in km) of the target - in this case Didymoon - and the impactor, and N is the number of projectiles. Fig. 4 (left) shows the size-frequency cumulative distribution of NEAs from Ivanov et al. (2002) that we have extrapolated to smaller sizes. The existing data are based on observations of impact craters on different bodies in the Solar System and are, therefore, limited since the craters with very low diameters are not spatially resolved by the common observation devices. The estimated impact frequency of meteoroids on Didymoon is shown in Fig. 4 (right). There are likely to be several impacts in the milligram to 10's of milligram range per year but very few impacts, if any, of 1 g mass and larger.

4.2. Thermal cracks and quakes

Large diurnal temperature excursions result in temperature cycles that can lead to mechanical load cycles producing stresses in surface rocks. Cracks can form and propagate due to temperature variations and the resulting temperature gradients set up by the thermal cycles. Recent laboratory experiments have shown that meteoritic material can fracture during typical thermal cycles experienced by asteroid surfaces (Delbo et al., 2014). The process of thermal cracking produces seismic signals that have already been observed in laboratory experiments (Yong and Wang, 1980; Vasin et al., 2006) and on the Moon during the Apollo missions (Duennebier and Merrill, 1976; Duennebier and Sutton, 1974; Latham et al., 1973; Sens-Schönfelder and Larose, 2010).

Acoustic emission is characterised by elastic (acoustic) waves propagating into the material following a sudden redistribution of internal stress and is a well known phenomenon in material analysis under macroscopic mechanical constraints. In general, the frequency range induced by such an excitation extends up to 0.5–1 MHz at the source (Arasteh et al., 1997), and the source time function can be approximated by a delta function with a duration of the order of a microsecond.

During the Apollo program widespread thermal events were detected with the seismometers. These thermal events are triggered by diurnal thermal stress changes. In addition, the source mechanism appears to be reactivated repeatedly producing almost identical signals at the same time of every lunation (Duennebier and Sutton, 1974; Sens-Schönfelder and Larose, 2010). The amplitudes of the observed individual thermal moonquake signals vary from less than 0.3 nm (peak to peak) to about 3 nm, an average value being about 0.6 nm (equivalent to an acceleration of 2.4 μm/s^2 at 10 Hz; Duennebier and Sutton, 1974).

In addition to these large, discrete thermal events observed on the Moon the ambient vibration produced by thermal stresses in the lunar environment can clearly be seen in Fig. 3 of Sens-Schönfelder and Larose (2010). The background noise measured on the four geophones deployed during the Apollo 17 mission show a close relation to the lunation period of 29.5 Earth days. The noise amplitude increases sharply just after sunrise and at dusk, with the highest energy levels being observed at sunset (Sens-Schönfelder and Larose, 2010). These signals are not individual seismic events, but rather the sum of the individual contributions (thermal micro-cracks), which cannot be separated. The region of emission is estimated to be in the kilometric range around the detection device (Nakamura, 1982). Despite the extended source of background thermal emission on the Moon, the measurements represent very low seismic displacements of typically 10–100 pm (accelerations of 40–400 nm/s^2 at 10 Hz). By considering the power spectra of the seismic data at different periods of the lunar day (night, morning and sunset) Sens-Schönfelder and Larose (2010), were able to determine that the frequency range of the thermal signal detectable on Apollo geophones is between 3 and 20 Hz, with a distinct maximum around 6–7 Hz. This observation clearly demonstrates that the signal emitted by thermal micro-cracks extends to frequencies well below the 10–100 kHz dominant frequency expected for such small sizes of fracture planes (Takatsubo and Kishi, 1990; Walter and Brune, 1993; Girard et al., 2013).

The seismic moment for a crack can be approximated as:

$$M_0 = \mu DA, \quad (2)$$

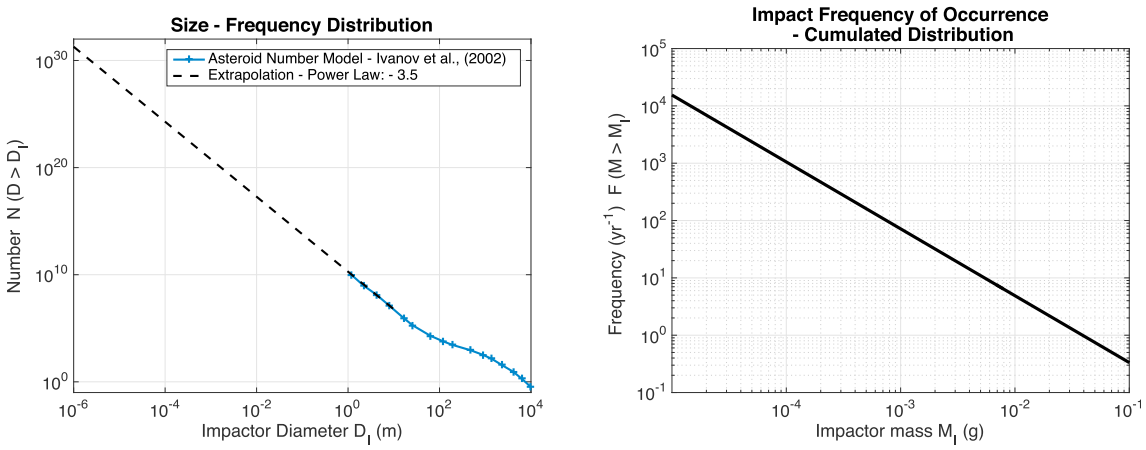

Fig. 4. NEA size distribution and impact frequency - (Left) The size-frequency cumulative distributions of NEAs from Ivanov et al. (2002) (solid line, crosses) and our power-law extrapolation to smaller sizes (dashed line). (Right) Estimated impact frequency for Didymoon as a function of the impactor mass. The diameter dependence of N is converted to mass assuming a density of 2.5×10^3 kg m^{-3}.

where D is the average displacement, A is the fault area and μ is the shear modulus of the material (Aki and Richards, 2002). From Eaton et al. (2014), for the specific case of shear rupture, this can be expressed in terms of the crack radius (a) and shear stress (σ_2):

$$M_0 = \frac{16}{7}\sigma_2 a^3, \tag{3}$$

and in the case of tensile rupture, this can be expressed in terms of the crack radius and the internal pressure (P_i):

$$M_0 = 2P_i a^3, \tag{4}$$

The amount of thermal cracking on Didymoon will depend on both the day/night thermal gradients and the rate of change of temperature at the surface. Fig. 5 compares typical surface temperature profiles on the Moon from Mazrouei et al. (2016) with those that we have calculated for Didymoon. Despite the fact that the temperature range is expected to be lower on Didymoon, the rate of change of temperature is much larger, due to the significantly faster rotation period. In the context of a seismic station on an asteroid surface, the shadowing of the lander may also create an even larger temperature contrast. This may generate large amplitude thermal cracking at close range. In addition, the lander itself may be subjected to thermal cracking and this could be a significant seismic source.

The thermal seismic signal is expected to be comparable to those already measured on the Moon but, due to the higher temporal thermal gradients, the seismic amplitudes are expected to be higher on Didymoon. The seismic energy will propagate across the asteroid with the high frequency components being diffracted and quickly attenuated. However, despite existing theoretical knowledge of both the seismic waves emitted by individual cracks (Walter and Brune, 1993; Eaton et al., 2014), and the time evolution of thermal cracks (Delbo et al., 2014), the relation between the surface thermal gradients and the spectral power of seismic signals has not yet been quantified.

4.3. *Tidal events*

Tidal interactions of small bodies during close planetary fly-bys may cause several structural phenomena in small bodies such as when a loosely consolidated rubble pile body is pulled apart into two or more components, sometimes forming crater chains e.g., (Bottke and Melosh, 1996; Schenk et al., 1996; Melosh and Whitaker, 1993). Tidal shear has also been studied as a possible formation mechanism of NEA binaries (Richardson et al., 1998b; Walsh and Richardson, 2006). In addition to the global modification a planetary body may undergo due to tidal forces, it has also been proposed that tidal stress on the surface of asteroids

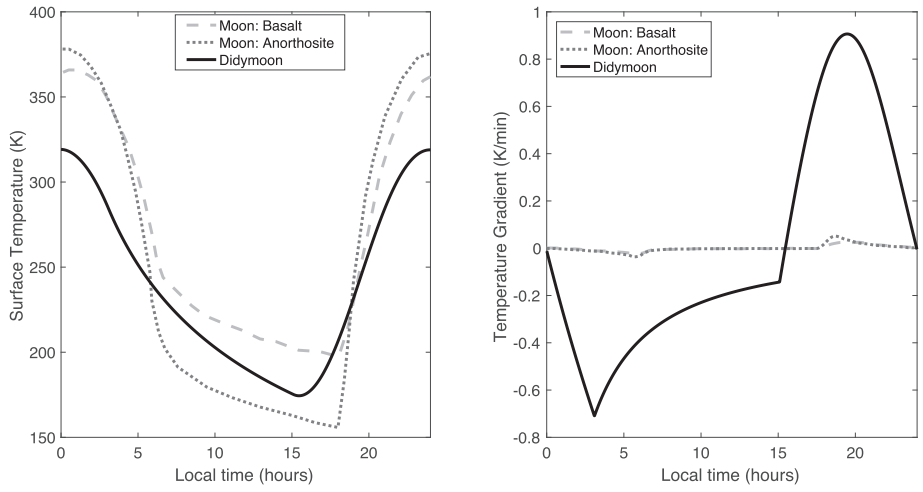

Fig. 5. Surface temperature variations - Surface temperature profiles for Basalt (typical in the lunar Maria) and Anorthosite Gabbro (typical in the lunar highlands) on the Moon from Mazrouei et al. (2016), compared with the typical temperature profiles for Didymoon. The figures are shown in local time for comparison, but one lunar day lasts 29.5 terrestrial days, while one local day on Didymoon lasts 12 h. This explains the increased temperature gradients found at the surface of Didymoon compared to the surface of the Moon.

during planetary encounters is strong enough to disturb and expose unweathered surface grains. This is, in fact, the most likely dominant short-term asteroid resurfacing process (Richardson et al., 1998b; Marchi et al., 2006; Binzel et al., 2010). The dynamical tidal environment of binary systems has also been studied in detail (Scheirich et al., 2015; Taylor and Margot, 2010; Goldreich and Sari, 2009). The surface of the Martian moon Phobos, for example, appears to be active and evolving as the global body deforms due to increasing tides related to orbital decay (Hurford et al., 2016). Additionally, deep moonquakes re-occur periodically in clusters in the Earth's Moon, suggesting tidal forcing (Nakamura, 2005; Latham et al., 1971; Bulow et al., 2007). The seismic moment from a microseism generated by tidal forcing may be described by the same equations as for the thermal crack (Section 4.2). In the following section we present a detailed study of the tidal stresses in Didymoon.

5. Tidal stresses in Didymoon

5.1. Failure criteria for geological materials

The Drucker-Prager model is common model for geological materials. As described in Holsapple (2007b), this model assumes that the allowable shear stress depends linearly on the confining pressure. Physically, that pressure dependence is the consequence of the interlocking of the granular particles, and not the friction on the surfaces of the particles. The Drucker-Prager failure criterion can be expressed as $J_2 = k - sI_1$, where k and s are material constants related to the cohesion, c (shear strength at zero pressure), and the angle of friction, ϕ, respectively. I_1 is the first invariant of the stress tensor ($I_1 = \sigma_1 + \sigma_2 + \sigma_3$, where σ_1, σ_2 and σ_3 are the normal stresses, with $\sigma_1 > \sigma_2 > \sigma_3$) and J_2 is the second invariant of the stress deviator tensor ($J_2 = \frac{1}{6}[(\sigma_1 - \sigma_2)^2 + (\sigma_2 - \sigma_3)^2 + (\sigma_3 - \sigma_1)^2 + \tau_{12}^2 + \tau_{23}^2 + \tau_{31}^2]$, where τ_{12}, τ_{23} and τ_{31} are the shear stresses).

Another failure criterion often used in geological studies is the Mohr-Coulomb failure criterion. Lay and Wallace (1995) describes it as the linear envelope in the principal stress plane on which an isotropic material will fail, while assuming the failure is only determined by σ_1 and σ_3. The Coulomb equation that gives the failure envelope at one point is $\tau = \sigma \tan\phi + c$. The Mohr-Coulomb criterion means, therefore, that for failure to happen, the shear stress (τ) must be greater than the combined cohesion (c) and normal stress (σ) acting on the material. In the case of tidal forcing in the Didymos system, the normal stress takes into account both the lithostatic pressure and the tidal stress.

The comparison between the Drucker-Prager and Mohr-Coloumb models is discussed in detail in Holsapple (2007b) who find that the differences between the two models are small. In the following we first apply the Drucker-Prager model to investigate how close Didymoon is to global failure (assuming a circular orbit), before using the Mohr-Coulomb model to study in detail the locations on Didymoon most susceptible to local failure (accounting for the ellipticity of the orbit but assuming a spherical asteroid). Finally, we discuss how the local failure may be modified by the ellipsoidal shape of Didymoon.

5.2. Didymoon tidal disruption limits

Based on the Drucker-Prager strength model and the analytical expressions developed by Holsapple and Michel (2006), we can determine the global disruption limit for a solid spinning body with zero cohesion subjected to tidal forces. These calculations assume the baseline properties of Didymoon (Section 3), and have been performed for both spherical and ellipsoidal shapes. In this model, Didymoon is assumed to be on a circular orbit (orbital eccentricity will be considered in the next section).

The criteria for disruption (global failure) to occur in the material is $\frac{J_2}{s^2 I_1^2} \geq 1$ and, therefore, the closer this value is to 1, the closer the body in question is to disruption. Shown in the left panel of Fig. 6 is the ratio $\frac{J_2}{s^2 I_1^2}$ for Didymoon, as a function of the angle of friction. The value of this ratio for Didymoon is also compared with that of the Earth's Moon and the Martian Moon Phobos (right panel of Fig. 6). Didymoon lies further from the disruption limit than Phobos, an object that already shows signs of tidal disruption at its surface (Hurford et al., 2016). However, Didymoon is much closer to the disruption limit than the Earth's Moon. Note that the Earth's Moon and Phobos are not cohesionless bodies and, therefore, will be further from the disruption limit than shown in this simplified example (the same may be true for Didymoon). Yet, as mentioned above, despite being far from the tidal disruption limit, tidal forcing in the Earth's Moon is still thought to be responsible for some lunar seismic activity.

5.3. Didymoon local tidal stress calculations

Here we assess the likelihood of tidally induced quakes occurring in Didymoon, and we include the eccentricity of Didymoon's orbit around Didymain. Tidal displacements are calculated based on the equations in the works of Alterman et al., (1959), Peltier and Andrews (Peltier and Andrews, 1976; Peltier, 1976), before being converted into stress. The internal structure models without voids considered (Figs. 2 and 3) are split into sublayers for numerical differentiation. The homogeneous model has one layer and 1000 equal sublayers, while the layered models have two layers (regolith and core), which are each split into 500 equal sublayers. The transition area between those two layers is also made of 500 equal sublayers, with a thickness of 20 cm. These values of sublayers were chosen since it guarantees convergence of our calculations in all the cases studied. For these calculations, unless otherwise stated, Didymoon is assumed to be a spherical body with zero cohesion, and with an angle of internal friction of 30°. Didymoon's orbital eccentricity is assumed to be 0.03 (Section 3).

Instead of working with seismic wave velocities and seismic attenuation, these calculations use the Lamé parameters and viscosity. As there is currently no clear consensus for determining the viscosity υ of a celestial body, we simplify the problem by using the seismic quality factor, Q, given in Section 3 to calculate the viscosity of Didymoon following the works of Miletich (2005): $\upsilon = \frac{KQ}{\omega}$, where K is the bulk modulus and ω is the orbital pulsation of Didymoon around Didymain. Our computations have been validated for an Earth's Moon model by comparison with previous results (Minshull and Goulty, 1988). Since viscosity variations between layers induce differential strains (and thus stresses) at the interfaces, the homogeneous model results are independent of the viscosity.

5.3.1. Didymoon tidal surface displacement

As a direct output of Alterman's equations (Alterman et al., 1959), the radial surface displacement (along u_r of Didymoon) has been calculated for all internal structure models without voids. It follows a sine-like function with a period equal to the orbital period of Didymoon around Didymain. The transverse surface displacement u_θ is also calculated in order to find the Love numbers h (linked to the radial displacement) and k (representing the potential change). Using the Love numbers, we can calculate the gravimetric factor $\gamma = 1 + h - \frac{3}{2}k$. Combining this with the variation in the gravitational potential from Alterman's equations, gives the variation of the surface gravity due to the orbital motion's eccentricity over the whole surface of Didymoon (Agnew, 2007). The values of the maximum amplitude of the surface displacement and variations in surface gravity at the equator and the poles are given in Table 1. As expected, the amplitudes are larger at the equator than at the poles, since the attraction of Didymain on Didymoon is stronger in the Didymain-facing equatorial area. Most of the surface displacement at the poles is an elastic counter-reaction to the elongation at the equator, because matter will contract in the direction orthogonal to the elongation.

5.3.2. Tidal stress in Didymoon

Differentiating the radial and horizontal displacements (Section 5.3.1) provides the strain over the entire body. This allows us to deduce

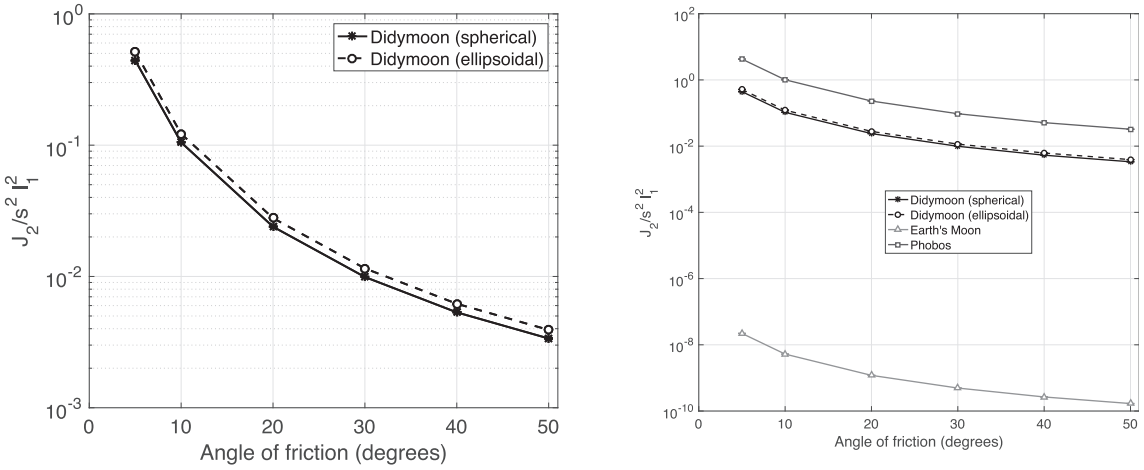

Fig. 6. The ratio of $\frac{J_2}{s^2 I_1^2}$ as a function of the angle of friction for (left) a spherical (dashed stars) and elliptical (solid circles) Didymoon, and (right) both Didymoon models, the Earth's Moon (grey triangles) and the Martian Moon Phobos (dark grey squares). If $\frac{J_2}{s^2 I_1^2} \geq 1$, then failure (plastic deformation) occurs in the material. The scatter in the Didymoon results due to the 30% uncertainty in the bulk density is approximately the size of the markers in the left figure. Typical dry granular materials will have angles of friction of 30–40°.

Table 1
Influence of the eccentricity of Didymoon's orbit around Didymain. The values shown are the maximum variations in the surface displacement and surface gravity experienced by Didymoon in an eccentric orbit, compared to Didymoon in a circular orbit around Didymain. For comparison, the local gravity at the surface of Didymoon is 48.88 μm/s^{-2} for the homogeneous models, 48.35 μm/s^{-2} for the 1 m regolith model and 44.11 μm/s^{-2} for the 10 m regolith model.

Models	Max. displacement variation (in *nm*)		Gravity variation (in nm/s^{-2})	
	Pole	Equator	Pole	Equator
Homogeneous model	−0.079	0.16	-3.8×10^{-6}	7.5×10^{-3}
1 m regolith model	−0.079	0.16	-3.7×10^{-6}	7.4×10^{-3}
10 m regolith model	−0.088	0.18	-3.4×10^{-6}	6.9×10^{-3}

the stress tensor at each point of Didymoon. In the case of a circular orbit, the radial stress would be largest at the equator on the near side of Didymoon (the side facing Didymain; longitude 0°) and on the far side of Didymoon (longitude 180°). Note that the longitudes are positive if they are eastwards, and are negative if westwards. The (0.03) orbital eccentricity means that maximum radial stresses are located closer to −4° and +176° in longitude since, in the elliptic case, the eccentric anomaly of Didymoon is $\frac{\pi}{2}$+ 0.03 rad (Fig. 7).

The difference of radial stress between the circular and eccentric orbits ($\Delta\sigma_r$) is found to be maximal at the equator at longitudes −30° and +150°, approximately, as shown in Fig. 8 a. Similarly, the colatitudinal stress variation between the circular and eccentric orbits ($\Delta\sigma_\theta$) is maximal at the same longitudes; however, as expected due to the symmetry of the problem, the colatitudinal stress variation is constant along a given meridian (Fig. 8 b). On the other hand, the difference of the longitudinal stress between the circular and eccentric orbits ($\Delta\sigma_\Phi$) has a maximum amplitude located at the poles, and also at different longitudes: +30° and −150°, approximately (Fig. 8 c).

5.3.3. *Tidal failure in Didymoon*

Diagonalisation of the stress tensor gives the absolute stress felt by Didymoon (including the tidal stresses and the lithostatic pressure). Then, by applying the Mohr-Coulomb failure criterion (as described in Section 5.1) we can see the regions of Didymoon where failure is the most likely to happen. Using the Mohr circle e.g., (Lay and Wallace, 1995), we can write the failure criterion as $\tau_m = \sigma_m \sin\phi + c\cos\phi$, where $\tau_m = (\sigma_3 - \frac{\sigma_1)}{2}$ is the maximal shear stress and $\sigma_m = (\sigma_3 + \frac{\sigma_1)}{2}$ is the maximal normal stress. Therefore, in the case of a cohesionless body, failure is reached when $\tau_m \geq \sigma_m \sin\phi$. Here we will call $C_{mc} = \sigma_m \sin\phi$, so that

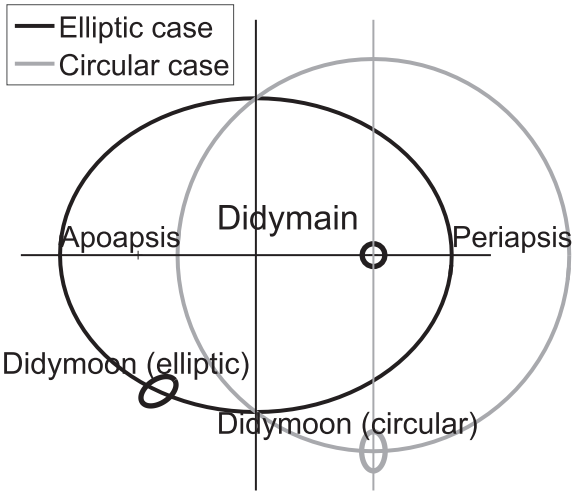

Fig. 7. Representation of the position of Didymoon on its orbit around Didymain for a mean anomaly of $\frac{\pi}{2}$ rad. If the orbit was circular (grey case), Didymoon would be right at $\frac{\pi}{2}$ rad with regard to Didymain; however, in the more realistic elliptic case (black case), Didymoon's eccentric anomaly is greater than $\frac{\pi}{2}$ rad. This graph is not to scale for neither Didymain, Didymoon nor the orbital parameters (the distance between the bodies is decreased, the eccentricity is increased).

failure is reached whenever $\tau_m \geq C_{mc}$, which is equivalent to $\tau_m - C_{mc} \geq 0$. Our simulations show that the part of the orbit where the stress is largest is when the mean anomaly is equal to $\frac{\pi}{2}$ and $-\frac{\pi}{2}$ rad (Fig. 9). Note that those stress values are given in the reference frame of the diagonalised stress tensor. Therefore, these are the maximum stresses an "ideally" orientated fault (i.e., a fault in the direction of the reference frame that diagonalises the stress tensor) would experience. Faults that are not orientated along this direction would experience weaker stresses.

For the homogeneous model failure first occurs at the poles (Fig. 8 d). This satisfies the spherical symmetry of the problem and is understandable as those are the regions where the shear stress is the strongest, the gravitational forces due to Didymain being tangent to the surface of Didymoon at this point. On the other hand, the regions where it is hardest for failure to occur are on the equator on Didymoon's near side (longitude 0°) and on the far side (longitude 180°), since it is principally the normal stresses acting at these places. We find that, for all values of the angle of friction (<1–50°), the surface stresses are strong enough to reach failure at the surface of the homogeneous model. For lower angles of friction, failure can occur not only at the surface but also even deeper (up to a

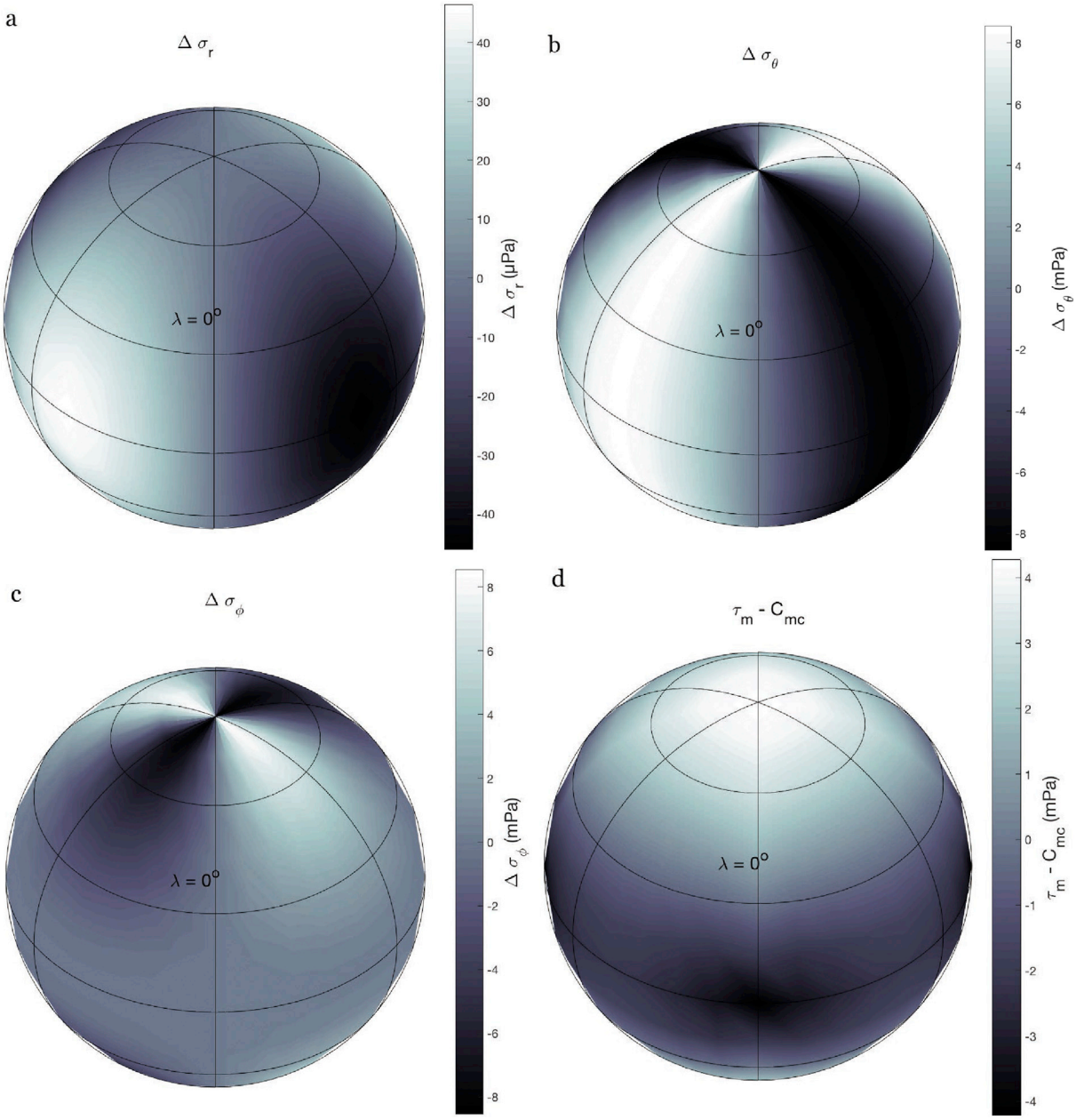

Fig. 8. Orthographic representation of the variations in the normal tidal stress at 8.15 cm depth in a homogeneous Didymoon. The panels indicate (a) the radial stress variation $\Delta\sigma_r$ (in μPa), (b) the longitudinal stress variation $\Delta\sigma_\theta$ (in mPa), and (c) the latitudinal stress variation $\Delta\sigma_\Phi$ (in mPa) experienced by Didymoon on an eccentric orbit, compared to Didymoon on a circular orbit around Didymain. (d) Shows the difference between the maximum shear stress τ_m and the failure criterion C_{mc}; a positive value indicates that failure is reached. Failure is seen to occur first at the poles (where τ_m - C_{mc} is at its maximum). The regions where it is hardest for failure to occur (where τ_m - C_{mc} is at its minimum) are on the equator facing Didymain (longitude 0°) and on the opposite face (longitude 180°). Stresses are plotted at 8.15 cm depth as this is the interface between the top two sub-layers in the homogeneous model. The value for the angle of friction is 30° and Didymain's position is located at the position of the reader (i.e., at 0°).

depth of 18 m for extremely low friction angles; Fig. 10).

The situation changes when one adds a regolith layer to the models. Didymoon models with regolith have a superficial, lower viscosity weak layer over a higher viscosity core. While the radial stress is continuous, the difference in viscosity between the two layers implies a stress drop in transverse directions between the core and the regolith. Because of its relative frailty and less viscous behaviour, the regolith layer dissipates those transverse stresses as transverse displacements. As a consequence, while horizontal displacements are greater, horizontal surface stresses are weaker than those in the homogeneous models. Since the horizontal surface stresses are the main source of shear, the consequence is that it is more difficult for a regolith-covered Didymoon to reach failure than for a homogeneous, consolidated Didymoon. Failure is, however, reached for the two regolith models (1 m and 10 m regolith depths), but at shallower locations, as seen in Fig. 10. While the presence of the regolith layer alters the values and repartition of stress over Didymoon, the poles are still the regions where failure is the most likely to happen.

5.3.4. *Influence of Didymoon ellipticity*

The models used in the detailed stress calculations above assume spherical, and layered bodies without any local inhomogeneity or anisotropy. As such, only the eccentricity of the orbit is taken into account, not the ellipticity of the secondary body. Here we discuss briefly the influence that the ellipsoidal shape of Didymoon may have on the above results.

The perturbation ψ of the total potential is calculated as the difference

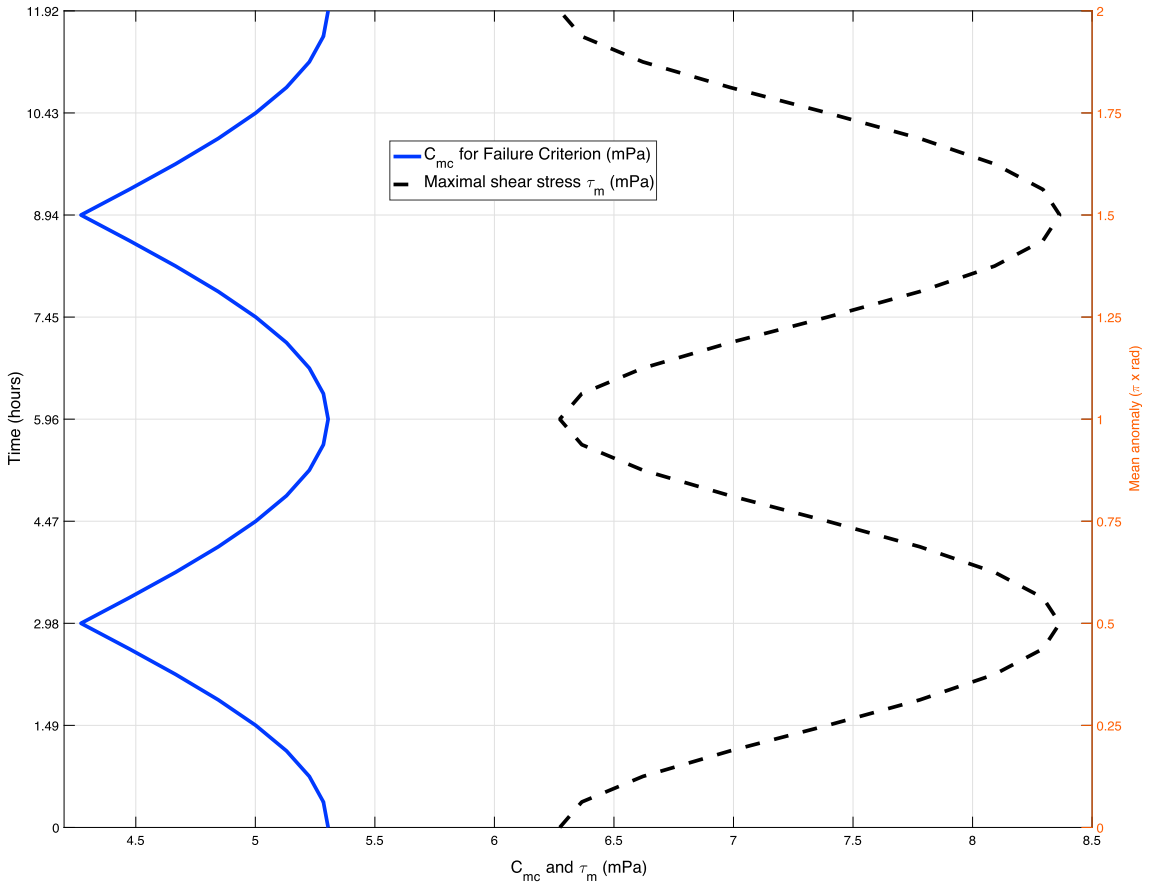

Fig. 9. Representation of the maximal shear stress in Didymoon τ_m (dashed line) and the required shear stress C_{mc} in order to reach local failure (solid line), as a function of time (left y-axis) and mean anomaly (right y-axis). The model of Didymoon used here is the homogeneous model. The failure is most easily reached when the difference between the maximal shear stress τ_m and the required shear stress C_{mc} is at its maximum. Such maxima are reached 3 h and 9 h after passing the periapsis (mean anomaly at $\frac{\pi}{2}$ and -$\frac{\pi}{2}$ rad).

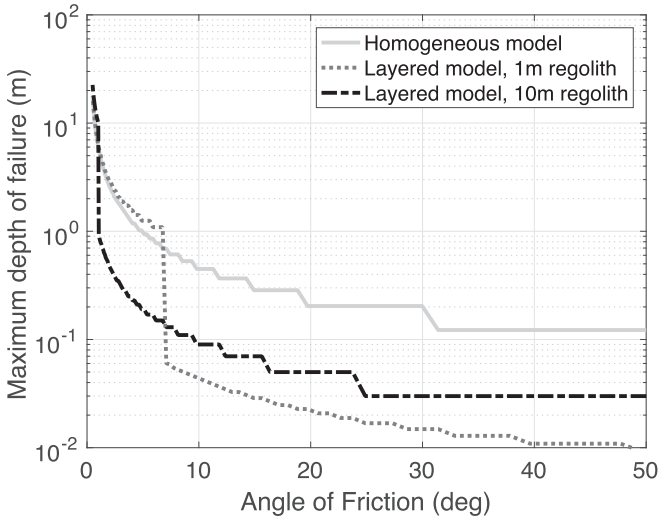

Fig. 10. Maximum depth of failure versus the angle of friction. Results are shown for the homogeneous Didymoon model (light grey solid line), the layered Didymoon model with a 1 m regolith (darker grey dotted line), and the layered Didymoon model with a 10 m regolith (black dashed line). The regular discontinuities are due to the quantification of the body into sub-layers of equal size. The spatial resolution varies between the models (see text), however, the depth of failure for large angles of friction always occurs between the upper two sub-layers in our models.

of the potential at a non-eccentric position and at the periapsis of the Didymoon's orbit around Didymain. Assuming a tidally-locked rotational state of the binary system, the gravitational potential of the Didymoon is constant in its frame of reference and its contribution to the perturbation ψ is, therefore, nil (as long as the other potentials do not significantly deform the body). The total potential considered here then includes the gravitational potential of Didymain, and the centrifugal potential (in the frame of reference of Didymoon).

The gradient of ψ is calculated along the meridian aligned with primary-secondary axis, at the surface of both a sphere and an ellipsoid ($a = 103$ m, $b = 79$ m and $c = 66$ m; Section 3), for comparison. The radial and the tangential components of the gradient of ψ are presented in Fig. 11 as a function of Θ; the angle between the furthest point from the primary asteroid and the considered point at the surface of Didymoon. The radial component curve for the spherical case shows that the body is stretched along the primary-secondary axis ($\Theta = 0°$ and $\Theta = \pm 180°$). At the poles ($\Theta = \pm 90°$), the radial component is nil, whereas the tangential one is close to its maximum amplitude. In the ellipsoid case, the curves show that this particular geometry tends to magnify the effects enlightened in the spherical case, by amplifying the stretching of the body on one hand, and by enlarging the area with high values of tangential component on the other hand. We can, therefore, conclude that the spherical analyses presented above are reasonable, but the effects may be larger in the case of an ellipsoidal Didymoon.

6. Seismic wave propagation in Didymoon

As discussed in detail above, seismic sources such as meteoroid impacts, as well as thermal cracks and tidally-induced events are expected to occur at the surface of Didymoon. In order to predict typical seismic waveforms for body and surface waves, possible reverberations and dispersive surface waves in case of a global regolith layer, as well as the

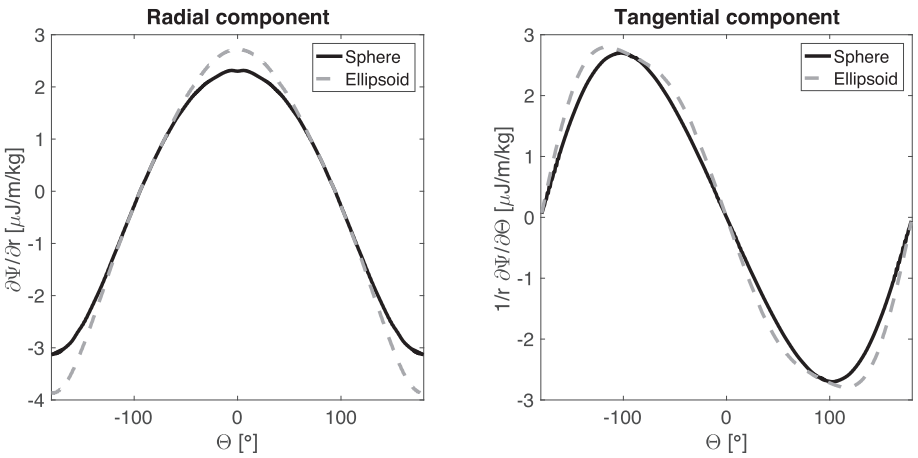

Fig. 11. Potential perturbation gradient - Radial (left) and tangential (right) components of the gravitational potential perturbation gradient for the sphere and the ellipsoid case ($a = 103$ m, $b = 79$ m, $c = 66$ m). The orbital eccentricity of Didymoon is $e = 0.03$. Θ is the angle between the furthest point from the primary asteroid and the considered point at the surface of Didymoon ($\Theta = \pm 180°$ points towards the primary).

effects of scattering heterogeneities within the body, we simulate the seismic wavefield for example seismic sources.

The seismic simulations use AxiSEM (Nissen-Meyer et al., 2014), which is based on an axisymmetric spherical geometry. This allows us to model the seismic wavefield with a higher resolution in time and space compared to former studies using normal mode modeling (e.g. Garcia et al., 2015) and compared to computationally expensive 3D approaches such as SPECFEM (Komatitsch and Tromp, 2002a, 2002b; Peter et al., 2011; Martin et al., 2008). AxiSEM also allows the inclusion of randomly or controlled distributed 2D heterogeneities such as voids and fractures to give a first estimate on the effect of heterogeneity as compared to a radial-symmetrically stratified asteroid. However, due to the axisymmetric setup, heterogeneities are transformed to concentric tubes within the body. The seismic wavefield is simulated for sources of equal energy at epicentral distances Δ between the receiver and its antipode at 1-degree steps.

6.1. *Influence of the internal structure on the seismic wave propagation*

The different seismic source types are described by their characteristic seismic moment, source time function or frequency content, and source mechanism. First, we consider a 1 mg meteoroid impactor with an impact velocity of 6 km/s. The impact source energy distribution is characterised by a Gaussian function, a seismic moment of 4.9e3 N.m (see Section 4) and a source duration of 5 ms (due to computational limitations, this is longer than the source duration predicted from theoretical calculations for a 1 mg impactor; see discussion in Section 6.2). As in Garcia et al. (2015), we assume a vertical impact, which can be

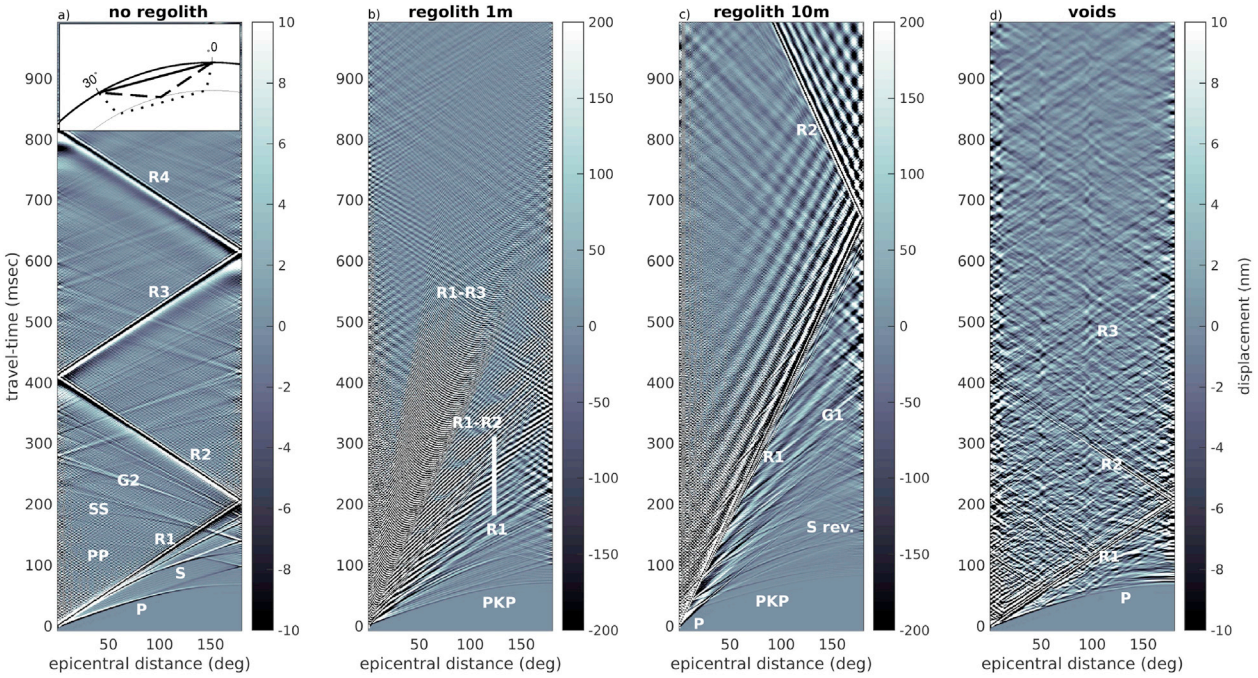

Fig. 12. Didymoon seismic wavefields - The vertical seismic wavefield for models with regolith thicknesses of a) 0, b) 1 and c) 10 m as well as, d) the asteroid containing voids of 5 m average diameter. The inset shows the ray paths of P (solid), PcP (dashed) and PKP (dotted) as predicted using the extended TauP Toolkit (Hempel and Garcia, in prep.). Marked phases include the body waves P and S, their multiples PP and SS, the core phase PKP, as well as the surface waves: Rayleigh waves (R1, R2 etc.) are non-dispersive for the homogeneous cases (a+d), but show clear dispersion for regolith layers. For a thin regolith, leakage of R1 into R2, R1 and R2 into R3 etc. can be observed (b). Reverberations are visible as thin lines shortly after the PKP phase (see also Fig. 13).

represented by an explosive source placed at the surface. This hypothesis is based on previous studies of small hypervelocity impacts that favour a seismic moment tensor close to that of an explosion (Walker and Huebner, 2004). Fig. 12 shows the resulting vertical seismic wavefields and Fig. 13 shows the waveforms for four hypothetical impacts of known locations at 30°, 90°, 120° and 150° epicentral distance. Computations are performed for the four internal structure models described in Fig. 2.

For a homogeneous spherical asteroid both P and S body waves, as well as the Rayleigh waves (R1, R2 etc.) traveling along the surface can be clearly observed. The surface waves travel several times around the tiny asteroid due to the low seismic attenuation. For a homogeneous body the surface waves are non-dispersive. For models with regolith layers on top of the asteroid's core, the surface waves become dispersive (Figs. 12 b + c, 14), allowing for the analysis of regolith thickness (discussed in Section 7). Also more complexity can be observed in the waveforms (Fig. 13): the thinner the regolith layer, the more reverberations of body waves can be observed. The seismic energy is effectively trapped in the regolith layer due to the strong impedance contrast at the regolith-core boundary. For a thicker regolith layer, the interference between reverberations is less destructive, hence the amplitudes of the waves traveling along the surface reach higher values than for a thinner regolith layer. With macro-porosity (voids) included, the seismic energy is more distributed over the entire wavefield. The onsets of seismic waves become less clear due to increased scattering (Figs. 12 d, 14). Little surface wave dispersion occurs for the internal structure model including voids. For all cases, the most prominent waves remain those traveling along the surface of the asteroid, and those focusing in the antipodal point of the seismic source ($\Delta = 180°$) and at the impact point itself after traveling 360°.

Zooming in on a few individual waveforms resulting from the different internal structure models (Fig. 13), we focus on the first arrivals. These are weak compared to the surface waves, thus we apply a time-dependent scaling function as described in Fig. 13. For a homogeneous asteroid, the first arrivals are clearly visible without considering the possibility of noise. Multiples of P and S, such as PP, SS, PPP, SSS would be the only other phases observable (Fig. 13).

For a thin regolith layer of 1 m thickness, the first arrival is directly followed by reverberations within the regolith layer. First arrivals are heavily delayed and decreased in amplitude for a thicker regolith layer of 10 m. For internal structure models including a regolith layer, direct body waves are only observable at very close distances, and core-phases such as PKP and SKS travel faster than the phases diffracted at the

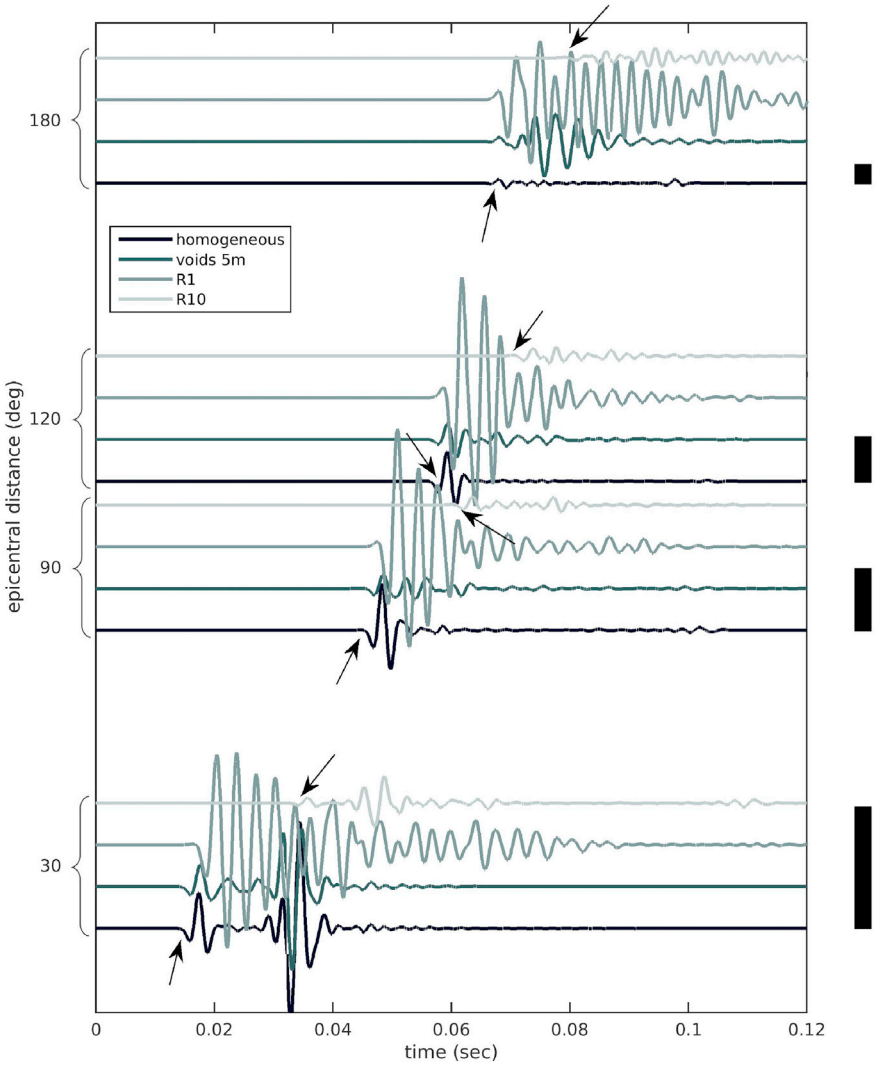

Fig. 13. Didymoon seismic waveforms - Seismic wave propagation computed at a time resolution of 5 ms for internal structure models with regolith thicknesses of 0, 1, and 10 m, as well as the asteroid containing voids of 5 m average diameter (see legend, and Fig. 2 for details about the internal structure models). The vertical seismic waveforms are recorded at 30°, 90°, 120° and 180° epicentral distance. To increase the visibility of the first arrivals, we suppressed the surface waves with a time-dependent scaling of $s(t) = \exp(-100(t-t_0(\Delta))$, where $t_0(\Delta)$ is the time of the first arrival of the P wave for the homogeneous asteroid. Arrows mark first arriving seismic phases: P and PKP (see inset of Fig. 12). Black bars give a scale of vertical ground motion per distance group.

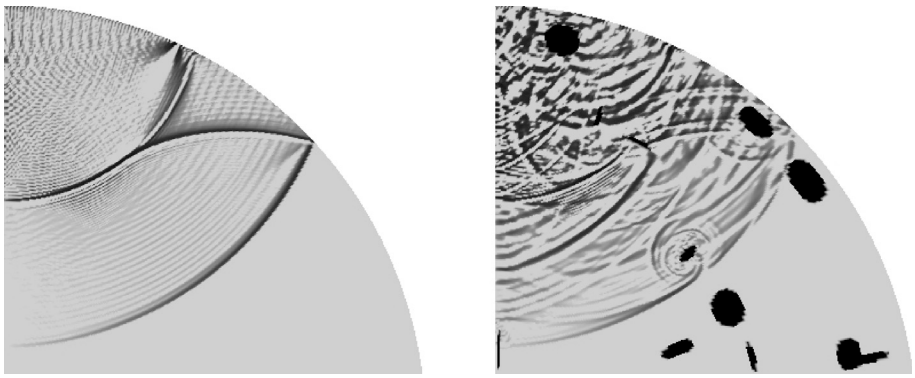

Fig. 14. Wavefront snapshots - (left) Wavefront for the model with 1 m of regolith. Here you can see the P as well as the S wave (concave wavefronts in the direction of propagation), their underside reflections PP and SS (convex wavefronts), as well as interference between the two. (Right) Wavefront for the model with randomly distributed 5 m voids. The wavefield becomes more complex, as increases slightly in period.

regolith-core boundary. In the case of the internal structure model with ≈7% macro-porosity, the first arrival are identifiable (Figs. 12 d and 13). In otherwords, for a strongly perturbed asteroid, first arrivals may be detected as long as both the seismic source is strong enough and the intrinsic attenuation is low enough to cause ground movements exceeding the self-noise level of the deployed instrument as well as possible environmental noise.

An analysis of the frequency content of the observed signal shows how the seismic amplitudes vary across the surface of Didymoon (Fig. 15 a). Compared to 90° epicentral distance, there is an increased amplitude near the impact site ($\Delta = 1°$) and at the antipodal point ($\Delta = 180°$). The influence of the internal structure is also visible in the spectra of the observed seismic signal (Fig. 15 b). Having a regolith layer increases the maximum of the acceleration spectrum by two orders of magnitude compared with the homogeneous model (due to the seismic energy trapped in the regolith layer). The interference is more destructive for the 1 m regolith case than for the 10 m regolith case resulting in lower amplitudes (particularly at lower frequencies) in the 1 m regolith case. Whereas the homogeneous structure results in a relatively smooth spectrum, small-scale structure such as a 1 m regolith layer and the voids result in a spectral response with multiple maxima. As there is no frequency-dependent absorption considered in these simulations, the peak of the spectra are determined by the source duration ($\tau = 5$ ms so the dominant source period is 200 Hz) and interference effects.

Concluding, we can discriminate between the four internal structure models easily: non-dispersive surface waves indicate the absence of a sharp boundary between regolith and core, whereas dispersive surface waves and strong reverberations indicate a clearly defined regolith layer. Analysis of either of these two observations would indicate the regolith thickness (see Section 7). Long coda indicates a laterally heterogeneous scattering interior. Not considering frequency-dependent absorption, shifts in frequency maxima are caused by interference. Thus, multiple maxima may indicate lateral heterogeneity.

6.2. *Influence of varying source characteristics*

Here we consider how the seismic source characteristics may influence the seismic signals. For a given internal structure model and epicentral distance, the spectral amplitude of the observed seismic signal varies linearly with the seismic moment. For example, for the homogeneous model at $\Delta = 90°$, the peak acceleration spectral amplitude, $A_{\max} \approx 2.4e6 * M_0$ for a vertical meteroid impact. As shown above (Fig. 15), the dominant observed frequency in our simulations is determined by the source duration. The source duration for a meteoroid impact (τ in seconds) can be obtained from scaling relations provided by Lognonné et al. (2009):

$$\tau = \left(\frac{8\pi^2 * 0.384 * S^2 m}{\varepsilon \rho V_p^3} \right)^{\left(\frac{1}{3}\right)} \tag{5}$$

where S is the seismic amplification (ranges from 0 to 2, or higher if there are ejecta), and ρ and V_p are respectively the density and the P-wave velocity of the target. This means that the smaller, more frequent impacts will lead to very short source durations and thus high dominant frequencies of the seismic wavefield (e.g., a 10 g and a 10 mg meteoroid will have dominant frequencies of ~1 kHz and ~10 kHz, respectively). Based

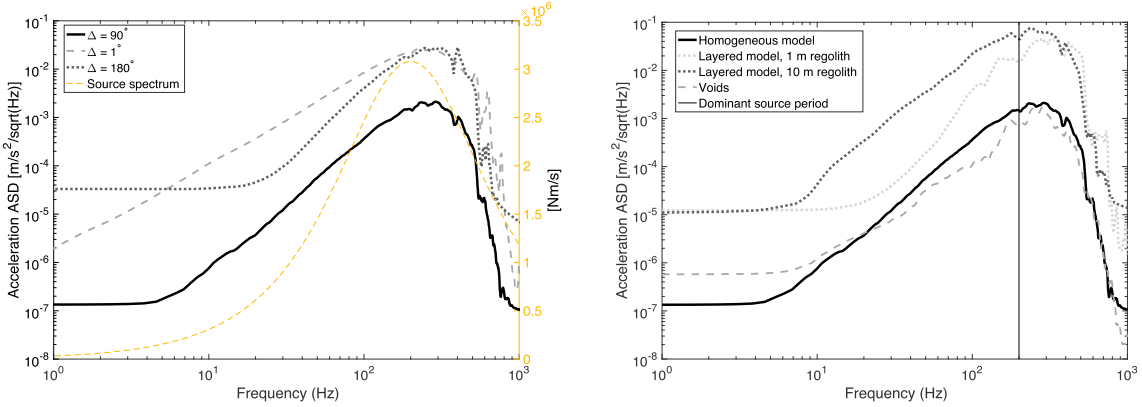

Fig. 15. Acceleration spectra - (a) Vertical ground acceleration amplitude spectral density for signals observed at $\Delta = 1°$, 90° and 180° for a 1 mg meteoroid impacting a homogeneous Didymoon at 6 km/s. (b) Vertical ground acceleration amplitude spectral density for signals observed at $\Delta = 90°$ for a 1 mg meteoroid impacting at 6 km/s. Four different internal structure models are considered (see Fig. 2). The vertical line marks the dominant source period of 200 Hz.

Table 2
Summary of the seismic measurement techniques for studying the internal structure of an asteroid with one three-component seismic station.

Method	Measurement requirement	Seismic analysis	Physical parameters	Assumptions	measurement depth
Coda analysis	Ground acceleration (3 axes) as a function of time including onset, maximum and at least part of the coda	Shape of the coda envelope as function of time Rise time measurement	$Q_i(f)$: Chemical composition, volatile content $Q_{Sc}(f)$: Estimate of mean size of sub-surface heterogeneities	Knowledge of the distance to the source and time of the source Absorption length > mean free path	Depends primarily on the attenuation. Penetration depth increases with decreasing attenuation.
H/V method	Ground acceleration (3 axes) of ambient noise	Peak of the H/V-spectra Ratio of the horizontal to vertical spectral amplitudes as a function of frequency (over full frequency band)	Thickness of the subsurface (regolith) layer, or average shear-wave velocity Layering and mechanical properties of the shallow sub-surface	Sharp reflector required i.e., assumes there is a regolith layer covering a more cohesive layer; Can be difficult to interpret data if there are significant lateral heterogeneities	Depends on the available frequency content and the velocity and attenuation structure
Receiver functions	Ground acceleration (3 axes) detecting at least a direct signal and a converted phase (reflection from seismic discontinuity)	Arrival times of converted phases, amplitudes (and waveforms)	Depths of discontinuities, velocity and density contrasts, and subsurface layering	Sharp reflector required i.e., assumes there is a regolith layer covering a more cohesive layer; Approximate knowledge of the source location	Can be deep (>30 m), gives only average information on shallow structure at length-scales below the seismic wavelengths

on this theoretical scaling, the source duration of 5 ms used above for a 1 mg impactor should have been much shorter. However, aforementioned effects of different structure models on seismic wavefield and the spectra, are qualitatively independent on the choice of source duration. Furthermore, we expect frequency-dependent absorption for any realistic asteroid structure. Hence, higher frequencies would be attenuated more efficiently than lower frequencies. However, since we only have constraints on Didymoon's density and an rough estimate on its composition, we chose to exclude assumptions of frequency-dependent absorption.

The seismic moment for one tidal or thermal crack can be estimated using Eq. (2). Considering a range of crack surface areas (1 cm^2 to 1 m^2) and maximum displacements (1 nm–10 cm), and using the shear wave velocity and density of lunar regolith to calculate the regolith shear modulus ($\mu = 240$ MPa; Cooper et al., 1974), this gives a range of seismic moments from 2.4e-5 to 2.4e7 N.m. Further analysis, therefore, has to be performed to estimate the typical seismic moment (and source duration) expected from tidally and thermally induced cracks before the range of expected observable signals can be determined.

7. Determining the internal structure of Didymoon using seismic measurements

Both the direct waves and signals in transmission, and the diffuse wavefield can be exploited to study the sub-surface and internal structure of the asteroid using in-situ seismic instrumentation. Our simulations above show the strong effect interior structure such as layering or random heterogeneities of length-scales between centimeters and meters have on the seismic amplitudes as well as the frequencies, and on the types of seismic phases that can be observed. If the first arrival is strong enough to be detected, it gives the average P wave velocity of the interior. The arrivals with the strongest amplitude, however, characterise the S wave properties of the uppermost layer. In the case where the asteroid can be simplified as an asteroid-core covered with a regolith layer, these measurements will allow the computation of seismic velocities as well as regolith thickness. Strong resonance frequencies or long coda will indicate either trapped waves or strong heterogeneity, respectively.

Here we discuss three additional measurement methods for studying the internal structure of an asteroid with one three-component seismic station: seismic coda analysis, H/V ratios, and receiver functions. Table 2 gives a short summary of the different methods and the physical parameters that can be obtained. These methods are then discussed in more detail below. Other methods, such exploiting the resonant modes of the asteroid, may also be useful but are not considered here.

7.1. Seismic coda analysis

The seismic coda refers to the scattered/diffuse wavefield i.e., the seismic signal past the arrival of the direct seismic phase. The shape of the envelope of the seismogram returns information on both the intrinsic attenuation (Q_i; the process of anelastic transformation of seismic energy to heat) as well as the apparent attenuation from the redirection of energy due to scattering (Q_{Sc}). The coda is characterised by its rise time and the characteristic decay time. The rise time is the delay in the arrival of the energy maximum due to scattering (Dainty and Toksoz, 1981). The rise time can be used to estimate the mean free path (approximately equivalent to the size of the scatterers) given that the intrinsic attenuation is weaker than the apparent attenuation due to scattering. The characteristic decay time τ_D, which is the time in which the coda amplitude decreases by a factor e, measures both Q_i and Q_{Sc}. Numerical modeling of the coda is necessary to discriminate between the effects of intrinsic attenuation and scattering (for an overview over these methods see Fig. 20 of Shearer, 2007). Measuring both the rise time and the shape of the coda envelope, i.e. the decay time, will provide information on the scattering and the absorption of the asteroid subsurface (e.g., Gillet et al., 2017). Usually, however, the coda decay is dominated by the absorption. Further discussion can be found in Blanchette-Guertin et al. (2012).

7.2. H/V method

On soft ground, horizontal motion is larger than vertical motion. However, on the hard ground, both horizontal and vertical motions are similar to each other both in the maximum value and waveform. Nakamura (1989) gives a method to study the sediment layer beneath the receiver using the frequency spectra of horizontal versus vertical components. The peak of this H/V-spectra is taken as the resonance frequency of the medium. Assuming that there is a strong impedance contrast ($\geq$2.5) between the sediment layer (the asteroid's regolith layer) and the underlying bedrock, the resonance frequency depends on the thickness of the sediment layer following a power law relation (Ibs-von Seht and Wohlenberg, 1999). The average shear-wave velocity v_S of a soft sedimentary layer, its thickness h and the resonance frequency f_R are approximately linked by $f_R = v_S/4h$ (see Delgado et al., 2000). Therefore, analysis of either the ambient noise or the coda detected on horizontal and vertical components can return valuable information about near-receiver shear wave velocity structure (mechanical properties) or regolith thickness, respectively.

7.3. Receiver functions

Receiver function analysis measures the depths beneath a seismic station due to teleseismic P or S wave energy partly converted to S or P waves at the discontinuity at a certain depth. This method is sensitive to the depths of layers as well as to the velocity structure beneath the seismometer and involves deconvolution of the source wavelet. Vinnik et al. (2001) shows the applicability of this method to the lunar seismic data. Receiver function analysis is also restricted by non-uniqueness of the seismic velocity model versus the layering model (Ammon et al., 1990). Furthermore, experiences with lunar data indicate that strong scattering would increase the difficulty of isolating individual receiver functions corresponding to individual depths or phases (Vinnik et al., 2001).

7.4. Additional techniques with multiple seismic stations

With two or more seismic stations, in addition to the techniques described above, the cross-correlation method can be applied using the diffuse wavefield, as long as there are continuous seismic records from the stations. If the seismic source is well located, and the station locations are known, the full seismic response of the asteroid will be provided. This means the body waves, the surface waves and the level of diffusion (i.e., heterogeneities). Analyzing the polarization of the diffuse wavefield should allow the determination of the direction of incoming wavefield. This means that, having a two or more seismic stations will also allow the seismic sources and diffraction sources to be localized. Finally, with several seismic stations, it may also be possible to determine the approximate location of a surface source using the direct body waves.

8. Conclusions

An in-situ seismic investigation on an asteroid could provide information about an asteroid's surface and interior properties. As there is evidence to suggest that asteroids are seismically active, passive rather than active seismology could be performed thus simplifying the mission design. In this paper, we have described the major natural seismic sources that may be present at Didymoon. Although meteoroid impacts are rare on an asteroid as small as Didymoon, thermal cracks and tidal stresses are expected to produce seismic signals. Based on our detailed tidal stress calculations, it is very likely that quakes occur on and in Didymoon due to failure from tidal stress, if Didymoon has an eccentric orbit. In both the homogeneous and the layered internal structure models that we have considered, failure is found to be reached first at the poles, and to occur close to the asteroid's surface.

Our simulations of seismic wave propagation have shown that a small (1 mg) meteoroid impacting a homogeneous Didymoon (at 6 km/s) can generate clearly observable body and surface waves that can travel several times around the tiny asteroid due to the low seismic attenuation. When a regolith layer is included, the seismic energy can become trapped in the regolith layer due to the strong impedance contrast at the regolith-core boundary. With macro-porosity (voids) included, the wavefield becomes more complex and the onsets of seismic waves become less clear due to increased scattering. Nonetheless, the most prominent waves remain those traveling along the surface of the asteroid and those focusing in the antipodal point of the seismic source.

Analysis of the waveforms and ground acceleration spectra allow discrimination between the different internal structure models. Seismic data recorded by just one station could, therefore, indicate the regolith thickness or lateral heterogeneity. In our simulations we have assumed a very conservative value for the seismic quality factor, providing lower bounds on the seismic wave amplitudes. In the future, a more realistic frequency-dependent absorption could also be included in the simulations and this is also likely to influence the spectra.

Ground accelerations from micrometeoroid impacts are large enough to cause lofting in the low-gravity asteroid environment. However, as found in Garcia et al. (2015), the vertical ground velocities are significantly smaller that the escape velocity, therefore, any unattached seismic station that is lofted will return to the surface. Additionally, given the low impact frequency of meteoroids, lower energy thermal cracks and tidally-induced seismic events are likely to be the dominant seismic sources at Didymoon. Lofting is, therefore, unlikely. However, if a seismic station was also equipped with an accelerometer, a lofting event would provide a unique opportunity to study the asteroid surface properties, perhaps at several locations if the lander bounces. An accelerometer could also provide information about the surface properties upon landing (e.g., Murdoch et al., 2017).

We have specifically considered micrometeoroid impacts, thermal cracks and tidal events, however, there may also be additional seismic sources that we have not yet considered such as downslope regolith motion cause by e.g., cliff collapse. Additionally, we have not yet taken into account the librations of Didymoon, so a next step would be to model the typical librations and integrate these into our tidal stresses analysis. The impact of the >300 kg DART spacecraft at ~7 km/s into Didymoon (Cheng et al., 2016) will also be a major seismic source. However, given the impact energy, it is likely that a (non-linear) shock wave will be generated in Didymoon and, considering the size of the impactor with respect to the target, this shock wave may fill the entire volume of the asteroid. Our elastic model cannot, therefore, be used to model the resulting wave propagation in Didymoon and hydrocodes (e.g., Asphaug et al., 1996b) should be used instead.

We have described several seismic measurement techniques that could be applied in order to study the asteroid internal structure with one three-component seismic station. Although the science return will be enhanced by having multiple seismic stations, one single seismic station can already vastly improve our knowledge about the seismic environment and sub-surface structure of an asteroid. In addition to performing the first surface-based geophysical investigation of an asteroid, a seismic experiment on Didymoon could lead to very unexpected and exciting scientific discoveries.

Acknowledgments

We gratefully acknowledge financial support from the French space agency (CNES) and the European Space Agency (ESA).

References

Agnew, D., 2007. Earth Tides, Treatise on Geophysics. In: Geodesy, Chapter Time Variable Gravity, Vol. 3. Elsevier Science, pp. 163–195.

AIM-A Team, 2015. Asteroid Impact Mission: Didymos Reference Model v10. ESA document reference: AD3-AIMA.

Aki, K., Richards, P.G., 2002. Quantitative Seismology, second ed. University Science Books.

Alterman, Z., Jarosch, H., Pekeris, C.L., 1959. Oscillations of the earth. Proc. R. Soc. A Math. Phys. Eng. Sci. 252 (1268), 80–95. http://dx.doi.org/10.1098/rspa.1959.0138. URL. http://rspa.royalsocietypublishing.org/cgi/doi/10.1098/rspa.1959.0138.

Ammon, C.J., Randall, G.E., Zandt, G., 1990. On the nonuniqueness of receiver function inversions. J. Geophys. Res. Solid Earth 95, 15. http://dx.doi.org/10.1029/JB095iB10p15303.

Arasteh, M., Chudnovsky, A., Dudley, J., Glaser, S., Ma, J., 1997. Broadband acoustic emission observations during fracture propagation in rock-like material. Int. J. Rock Mech. Min. Sci. 34 (3), 83.e1–83.e13. http://dx.doi.org/10.1016/S1365-1609(97)00205-0. URL. http://www.sciencedirect.com/science/article/pii/S1365160997002050.

Asphaug, E., 2008. Critical crater diameter and asteroid impact seismology. Meteorit. Planet. Sci. 43, 1075–1084. http://dx.doi.org/10.1111/j.1945-5100.2008.tb00694.x.

Asphaug, E., Moore, J.M., Morrison, D., Benz, W., Nolan, M.C., Sullivan, R.J., 1996. Mechanical and geological effects of impact cratering on Ida. Icarus 120 (1), 158–184. http://dx.doi.org/10.1006/icar.1996.0043. URL. http://www.sciencedirect.com/science/article/pii/S0019103596900433.

Asphaug, E., Moore, J.M., Morrison, D., Benz, W., Nolan, M.C., Sullivan, R.J., 1996. Mechanical and geological effects of impact Cratering on Ida. Icarus 120 (1), 158–184. http://dx.doi.org/10.1006/icar.1996.0043. URL. http://www.sciencedirect.com/science/article/pii/S0019103596900433.

Asphaug, E., King, P., Swift, M., Merrifield, M., 2001. Brazil nuts on Eros: size-sorting of Asteroid Regolith. In: Lunar and Planetary Science Conference, p. 1708 no. 32.

Besse, S., Küppers, M., Barnouin, O., Thomas, N., Benkhoff, J., 2014. Lutetia's lineaments. Planet. Space Sci. 101, 186–195. http://dx.doi.org/10.1016/j.pss.2014.07.007. URL. http://www.sciencedirect.com/science/article/pii/S0032063314002037.

Binzel, R.P., Morbidelli, A., Merouane, S., DeMeo, F.E., Birlan, M., Vernazza, P., Thomas, C.A., Rivkin, A.S., Bus, S.J., Tokunaga, A.T., 2010. Earth encounters as the origin of fresh surfaces on near-Earth asteroids. Nature 463, 331–334. http://dx.doi.org/10.1038/nature08709.

Blanchette-Guertin, J.-F., Johnson, C.L., Lawrence, J.F., 2012. Investigation of scattering in lunar seismic coda. J. Geophys. Res. (Planets) 117, E06003. http://dx.doi.org/10.1029/2011JE004042.

Bottke, W.F., Melosh, H.J., 1996. Formation of asteroid satellites and doublet craters by planetary tidal forces. Nature 381, 51–53.

Bottke Jr., W.F., Nolan, M.C., Greenberg, R., Kolvoord, R.A., 1994. Collisional lifetimes and impact statistics of near-earth Asteroids. In: Gehrels, T., Matthews, M.S., Schumann, A.M. (Eds.), Hazards Due to Comets and Asteroids, p. 337.

Britt, D., Consolmagno, G., 2000. The porosity of dark meteorites and the structure of low-albedo asteroids. Icarus 146 (1), 213–219. http://dx.doi.org/10.1006/icar.2000.6374. URL. http://www.sciencedirect.com/science/article/pii/S0019103500963747.

Buczkowski, D.L., Wyrick, D.Y., Iyer, K.A., Kahn, E.G., Scully, J.E.C., Nathues, A., Gaskell, R.W., Roatsch, T., Preusker, F., Schenk, P.M., Le Corre, L., Reddy, V., Yingst, R.A., Mest, S., Williams, D.A., Garry, W.B., Barnouin, O.S., Jaumann, R., Raymond, C.A., Russell, C.T., 2012. Large-scale troughs on Vesta: A signature of planetary tectonics. Geophys. Rev. Lett. 39, L18205. http://dx.doi.org/10.1029/2012GL052959.

Bulow, R.C., Johnson, C.L., Bills, B.G., Shearer, P.M., 2007. Temporal and spatial properties of some deep moonquake clusters. J. Geophys. Res. (Planets) 112, E09003. http://dx.doi.org/10.1029/2006JE002847.

Carry, B., 2012. Density of Asteroids. ArXiv e-printsarXiv:1203.4336. http://dx.doi.org/10.1016/j.pss.2012.03.009.

Cheng, A.F., 2002. Near Earth Asteroid Rendezvous: Mission Summary, Asteroids III, pp. 351–366.

Cheng, A.F., Izenberg, N., Chapman, C.R., Zuber, M.T., 2002. Ponded deposits on asteroid 433 Eros. Meteorit. Planet. Sci. 37, 1095–1105.

Cheng, A.F., Michel, P., Jutzi, M., Rivkin, A.S., Stickle, A., Barnouin, O., Ernst, C., Atchison, J., Pravec, P., Richardson, D.C., 2016. Asteroid impact & deflection assessment mission: kinetic impactor. Planet. Space Sci. 121, 27–35. http://dx.doi.org/10.1016/j.pss.2015.12.004.

Consolmagno, G., Britt, D., Macke, R., 2008. The significance of meteorite density and porosity. Chem. Erde/Geochem. 68, 1–29. http://dx.doi.org/10.1016/j.chemer.2008.01.003.

Cooper, M.R., Kovach, R.L., Watkins, J.S., 1974. Lunar near-surface structure. Rev. Geophys. Space Phys. 12, 291–308. http://dx.doi.org/10.1029/RG012i003p00291.

Dainty, A.M., Toksoz, M.N., 1981. Seismic codas on the earth and the moon - A comparison. Phys. Earth Planet. Interiors 26, 250–260. http://dx.doi.org/10.1016/0031-9201(81)90029-7.

de Leon, J., Licandro, J., Serra-Ricart, M., Pinilla-Alonso, N., Campins, H., 2010. Observations, compositional, and physical characterizationof near-earth and mars-crosser asteroids from a spectroscopic survey. Astronomy Astrophys. 517, A23. http://dx.doi.org/10.1051/0004-6361/200913852.

Delbo, M., Libourel, G., Wilkerson, J., Murdoch, N., Michel, P., Ramesh, K.T., Ganino, C., Verati, C., Marchi, S., 2014. Thermal fatigue as the origin of regolith on small asteroids. Nature 508, 233–236. http://dx.doi.org/10.1038/nature13153.

Delgado, J., López Casado, C., Giner, J., Estévez, A., Cuenca, A., Molina, S., 2000. Microtremors as a geophysical exploration tool: applications and limitations. Pure Appl. Geophys. 157, 1445–1462.

DeMeo, F.E., Alexander, C.M.O., Walsh, K.J., Chapman, C.R., Binzel, R.P., 2015. The Compositional Structure of the Asteroid Belt, pp. 13–41.

Dombard, A.J., Freed, A.M., 2002. Thermally induced lineations on the asteroid Eros: evidence of orbit transfer. Geophys. Res. Lett. 29 (16) http://dx.doi.org/10.1029/2002GL015181.

Duennebier, F., 1976. Thermal movement of the regolith. In: Merrill, R.B. (Ed.), Lunar and Planetary Science Conference Proceedings, pp. 1073–1086. Vol. 7 of Lunar and Planetary Science Conference Proceedings.

Duennebier, F., Sutton, G.H., 1974. Thermal moonquakes. J. Geophys. Res. 79, 4351–4363. http://dx.doi.org/10.1029/JB079i029p04351.

Eaton, D.W., van der Baan, M., Birkelo, B., Tary, J.-B., 2014. Scaling relations and spectral characteristics of tensile microseisms: evidence for opening/closing cracks during hydraulic fracturing. Geophys. J. Int. 196, 1844–1857. http://dx.doi.org/10.1093/gji/ggt498.

Edwards, W.N., Eaton, D.W., Brown, P.G., 2008. Seismic observations of meteors: coupling theory and observations. Rev. Geophys. 46, 4007. http://dx.doi.org/10.1029/2007RG000253.

Fujiwara, A., Kawaguchi, J., Yeomans, D.K., Abe, M., Mukai, T., Okada, T., Saito, J., Yano, H., Yoshikawa, M., Scheeres, D.J., Barnouin-Jha, O., Cheng, A.F., Demura, H., Gaskell, R.W., Hirata, N., Ikeda, H., Kominato, T., Miyamoto, H., Nakamura, A.M., Nakamura, R., Sasaki, S., Uesugi, K., 2006. The Rubble-Pile Asteroid Itokawa as observed by Hayabusa. Science 312 (5778), 1330–1334. http://dx.doi.org/10.1126/science.1125841 arXiv: http://www.sciencemag.org/cgi/reprint/312/5778/1330.pdf http://www.sciencemag.org/cgi/content/abstract/312/5778/1330. URL.

Gagnepain-Beyneix, J., Lognonné, P., Chenet, H., Lombardi, D., Spohn, T., 2006. A seismic model of the lunar mantle and constraints on temperature and mineralogy. Phys. Earth Planet. Interiors 159, 140–166. http://dx.doi.org/10.1016/j.pepi.2006.05.009.

Garcia, R.F., Murdoch, N., Mimoun, D., 2015. Micro-meteoroid seismic uplift and regolith concentration on kilometric scale asteroids. Icarus 253, 159–168. http://dx.doi.org/10.1016/j.icarus.2015.02.014.

Gardner, G., Gardner, L., Gregory, A., 1974. Formation velocity and density-the diagnostic basics for stratigraphic traps. Geophysics 39 (6), 770–780.

Gillet, K., Margerin, L., Calvet, M., Monnereau, M., 2017. Scattering attenuation profile of the Moon: implications for shallow moonquakes and the structure of the megaregolith. Phys. Earth Planet. Interiors 262, 28–40. http://dx.doi.org/10.1016/j.pepi.2016.11.001.

Girard, L., Gruber, S., Weber, S., Beutel, J., 2013. Environmental controls of frost cracking revealed through in situ acoustic emission measurements in steep bedrock. Geophys. Res. Lett. 40, 1748–1753. http://dx.doi.org/10.1002/grl.50384.

Goldreich, P., Sari, R., 2009. Tidal evolution of rubble piles. Astrophys. J. 691, 54–60. http://dx.doi.org/10.1088/0004-637X/691/1/54. arXiv:0712.0446.

Gonzalez, J.A., Bello, M., Martin-Albo, J.F., Galvez, A., 2004. Don Quijote: An ESA mission for the assessment of the NEO threat. In: International Astronautical Congress. Paper IAC-04-Q.P.21.

Graps, A.L., Blondel, P., Bonin, G., Britt, D., Centuori, S., Delbo, M., Drube, L., Duffard, R., Elvis, M., Faber, D., Frank, E., Galache, J., Green, S.F., Thimo Grundmann, J., Hsieh, H., Kereszturi, A., Laine, P., Levasseur-Regourd, A.-C., Maier, P., Metzger, P., Michel, P., Mueller, M., Mueller, T., Murdoch, N., Parker, A., Pravec, P., Reddy, V., Sercel, J., Rivkin, A., Snodgrass, C., Tanga, P., ASIME 2016 White Paper: In-space Utilisation of Asteroids: "Answers to Questions from the Asteroid Miners", ArXiv e-printsarXiv: 1612.00709.

Harris, A.W., Fahnestock, E.G., Pravec, P., 2009. On the shapes and spins of "rubble pile" asteroids. Icarus 199, 310–318. http://dx.doi.org/10.1016/j.icarus.2008.09.012.

Hempel, S., Garcia, R.F., The extended taup toolkit incl. prediction of amplitudes, ellipticity, topography and crustal thickness corrections for earth and other planets, submitted to Seismological Research Letters, (In Prep.).

Holsapple, K.A., 2007. Spin limits of solar system bodies: from the small fast-rotators to 2003 EL61. Icarus 187, 500–509. http://dx.doi.org/10.1016/j.icarus.2006.08.012.

Holsapple, K.A., 2007. Spin limits of solar system bodies: from the small fast-rotators to 2003 EL61. Icarus 187 (2), 500–509. http://dx.doi.org/10.1016/j.icarus.2006.08.012. URL. http://www.sciencedirect.com/science/article/pii/S0019103506002776.

Holsapple, K.A., 2013. Modeling granular material flows: the angle of repose, fluidization and the cliff collapse problem. Planet. Space Sci. 82–83, 11–26. http://dx.doi.org/10.1016/j.pss.2013.03.001. URL. http://www.sciencedirect.com/science/article/pii/S0032063313000573.

Holsapple, K.A., Michel, P., 2006. Tidal disruptions: A continuum theory for solid bodies. Icarus 183, 331–348. http://dx.doi.org/10.1016/j.icarus.2006.03.013.

Horvath, P., Latham, G.V., Nakamura, Y., Dorman, H.J., 1980. Lunar near-surface shear wave velocities at the Apollo landing sites as inferred from spectral amplitude ratios. Geophys. Res. Lett. 85, 6572–6578. http://dx.doi.org/10.1029/JB085iB11p06572.

Housen, K.R., Holsapple, K.A., 2003. Impact cratering on porous asteroids. Icarus 163, 102–119. http://dx.doi.org/10.1016/S0019-1035(03)00024-1.

Hurford, T.A., Asphaug, E., Spitale, J.N., Hemingway, D., Rhoden, A.R., Henning, W.G., Bills, B.G., Kattenhorn, S.A., Walker, M., 2016. Tidal disruption of phobos as the cause of surface fractures. J. Geophys. Res. Planets. http://dx.doi.org/10.1002/2015JE004943.

Ibs-von Seht, M., Wohlenberg, J., 1999. Microtremor measurements used to map thickness of soft sediments. Bull. Seismol. Soc. Am. 89 (1), 250–259 arXiv: http://bssa.geoscienceworld.org/content/89/1/250.full.pdf http://bssa.geoscienceworld.org/content/89/1/250. URL.

Ivanov, B.A., Neukum, G., Bottke Jr., W.F., Hartmann, W.K., 2002. The Comparison of Size-frequency Distributions of Impact Craters and Asteroids and the Planetary Cratering Rate, pp. 89–101.

Jaumann, R., Williams, D.A., Buczkowski, D.L., Yingst, R.A., Preusker, F., Hiesinger, H., Schmedemann, N., Kneissl, T., Vincent, J.B., Blewett, D.T., Buratti, B.J., Carsenty, U., Denevi, B.W., De Sanctis, M.C., Garry, W.B., Keller, H.U., Kersten, E., Krohn, K., Li, J.-

Y., Marchi, S., Matz, K.D., McCord, T.B., McSween, H.Y., Mest, S.C., Mittlefehldt, D.W., Mottola, S., Nathues, A., Neukum, G., O'Brien, D.P., Pieters, C.M., Prettyman, T.H., Raymond, C.A., Roatsch, T., Russell, C.T., Schenk, P., Schmidt, B.E., Scholten, F., Stephan, K., Sykes, M.V., Tricarico, P., Wagner, R., Zuber, M.T., Sierks, H., 2012. Vesta's shape and morphology. Science 336, 687. http://dx.doi.org/10.1126/science.1219122.

Jutzi, M., Benz, W., Michel, P., 2008. Numerical simulations of impacts involving porous bodies. I. Implementing sub-resolution porosity in a 3D SPH hydrocode. Icarus 198, 242–255. http://dx.doi.org/10.1016/j.icarus.2008.06.013.

Kedar, S., Richardson, J., Harvey, N., Perry, D., Bowling, T., Webb, F., Kanamori, H., Garnero, E., 2012. Laboratory simulations of maritan meteorite impacts and their seismic signatures: how hard do we need to hit mars to see what it's made of?. In: AGU Fall Meeting 2012.

Komatitsch, D., Tromp, J., 2002. Spectral-element simulations of global seismic wave propagationi. validation. Geophys. J. Int. 149 (2), 390–412.

Komatitsch, D., Tromp, J., 2002. Spectral-element simulations of global seismic wave propagationii. three-dimensional models, oceans, rotation and self-gravitation. Geophys. J. Int. 150 (1), 303–318.

Latham, G., Ewing, M., Dorman, J., Lammlein, D., Press, F., Toksoz, N., Sutton, G., Duennebier, F., Nakamura, Y., 1971. Moonquakes. Science 174, 687–692. http://dx.doi.org/10.1126/science.174.4010.687.

Latham, G.V., Ewing, M., Press, F., Dorman, J., Nakamura, Y., Toksoz, N., Lammlein, D., Duennebier, F., Dainty, A., 1973. Passive seismic experiment. In: Apollo 17: Preliminary Science Report, p. 11. Vol. 330 of NASA Special Publication.

Lay, T., Wallace, T.C., 1995. Modern Global Seismology. Academic Press google-Books-ID: CSCuMPt5CTcC.

Lognonné, P., Le Feuvre, M., Johnson, C.L., Weber, R.C., 2009. Moon meteoritic seismic hum: steady state prediction. J. Geophys. Res. (Planets) 114, 12003. http://dx.doi.org/10.1029/2008JE003294.

Marchi, S., Magrin, S., Nesvorný, D., Paolicchi, P., Lazzarin, M., 2006. A spectral slope versus perihelion distance correlation for planet-crossing asteroids. MNRAS 368, L39–L42. http://dx.doi.org/10.1111/j.1745-3933.2006.00152.x.

Martin, R., Komatitsch, D., Blitz, C., Le Goff, N., 2008. Simulation of seismic wave propagation in an asteroid based upon an unstructured mpi spectral-element method: blocking and non-blocking communication strategies. In: High Performance Computing for Computational Science-VECPAR 2008. Springer, pp. 350–363.

Mazrouei, S., Ali Lagoa, V., Delbo, M., Ghent, R.R., Wilkerson, J., 2016. Does thermal fatigue play a role in lunar Regolith formation?. In: Lunar and Planetary Science Conference, p. 1785. Vol. 47 of Lunar and Planetary Science Conference.

Melosh, H.J., Whitaker, E.A., 1993. Lunar crater chains. Nature 365, 713.

Michel, P., Benz, W., Tanga, P., Richardson, D.C., 2001. Collisions and gravitational reaccumulation: forming asteroid families and satellites. Science 294, 1696–1700. http://dx.doi.org/10.1126/science.1065189.

Michel, P., O'Brien, D.P., Abe, S., Hirata, N., 2009. Itokawa's cratering record as observed by Hayabusa: implications for its age and collisional history. Icarus 200, 503–513. http://dx.doi.org/10.1016/j.icarus.2008.04.002.

Michel, P., Cheng, A., Kuippers, M., Pravec, P., Blum, J., Delbo, M., Green, S., Rosenblatt, P., Tsiganis, K., Vincent, J., Biele, J., Ciarletti, V., Hérique, A., Ulamec, S., Carnelli, I., Galvez, A., Benner, L., Naidu, S., Barnouin, O., Richardson, D., Rivkin, A., Scheirich, P., Moskovitz, N., Thirouin, A., Schwartz, S., Bagatin, A.C., Yu, Y., 2016. Science case for the asteroid impact mission (aim): A component of the asteroid impact and deflection assessment (aida) mission. Adv. Space Res. 57 (12), 2529–2547. http://dx.doi.org/10.1016/j.asr.2016.03.031.

Miletich, R., 2005. Mineral Behaviour at Extreme Conditions, the Mineralogical Society of Great Britain and Ireland (google-Books-ID: ftqGCgAAQBAJ).

Minshull, T., Goulty, N., 1988. The influence of tidal stresses on deep moonquake activity. Phys. Earth Planet. Interiors 52 (1–2), 41–55. http://dx.doi.org/10.1016/0031-9201(88)90056-8. URL. http://linkinghub.elsevier.com/retrieve/pii/0031920188900568.

Miyamoto, H., Yano, H., Scheeres, D.J., Abe, S., Barnouin-Jha, O., Cheng, A.F., Demura, H., Gaskell, R.W., Hirata, N., Ishiguro, M., Michikami, T., Nakamura, A.M., Nakamura, R., Saito, J., Sasaki, S., 2007. Regolith migration and sorting on asteroid Itokawa. Science 316 (5827), 1011–1014. http://dx.doi.org/10.1126/science.1134390 arXiv: http://www.sciencemag.org/cgi/reprint/316/5827/1011.pdf http://www.sciencemag.org/cgi/content/abstract/316/5827/1011. URL.

Murchie, S., Robinson, M., Clark, B., Li, H., Thomas, P., Joseph, J., Bussey, B., Domingue, D., Veverka, J., Izenberg, N., Chapman, C., 2002. Color variations on Eros from NEAR multispectral imaging. Icarus 155, 145–168. http://dx.doi.org/10.1006/icar.2001.6756.

Murdoch, N., Sanchez, P., Schwartz, S., Miyamoto, H., 2015. Asteroid surface geophysics. In: Michel, P., DeMeo, F.E., Bottke, W.F. (Eds.), Asteroids IV, Space Science Series.

Murdoch, N., Avila Martinez, I., Sunday, C., Zenou, E., Cherrier, O., Cadu, A., Gourinat, Y., 2017. An experimental study of low-velocity impacts into granular material in reduced gravity. Mon. Not. R. Astron. Soc. 468 (2), 1259–1272. http://dx.doi.org/10.1093/mnras/stw3391.

Nakamura, Y., 1982. Apollo lunar seismic experiment - final summary. In: Lunar and Planetary Science Conference, pp. 576–577. Vol. 13 of Lunar and Planetary Science Conference.

Nakamura, Y., 1989. A Method for Dynamic Characteristics Estimation of Subsurface Using Microtremor on Ground Surface, QR of RTRI, pp. 25–33.

Nakamura, Y., 2005. Farside deep moonquakes and deep interior of the Moon. J. Geophys. Res. (Planets) 110, E01001. http://dx.doi.org/10.1029/2004JE002332.

Nissen-Meyer, T., van Driel, M., Stähler, S., Hosseini, K., Hempel, S., Auer, L., Colombi, A., Fournier, A., 2014. Axisem: broadband 3-d seismic wavefields in axisymmetric media. Solid earth.. 5 (1), 425.

O'Brien, D.P., Sykes, M.V., Tricarico, P., 2011. Collision probabilities and impact velocity distributions for vesta and ceres. In: Lunar and Planetary Science Conference, p. 2665. Vol. 42 of Lunar and Planetary Science Conference.

Peltier, W.R., 1976. Glacial-isostatic adjustmentII. The inverse problem. Geophys. J. R. Astronomical Soc. 46 (3), 669–705. http://dx.doi.org/10.1111/j.1365-246X.1976.tb01253.x. URL. http://onlinelibrary.wiley.com/doi/10.1111/j.1365-246X.1976.tb01253.x/abstract.

Peltier, W.R., Andrews, J.T., 1976. Glacial-isostatic adjustmenti. the forward problem. Geophys. J. R. Astronomical Soc. 46 (3), 605–646. http://dx.doi.org/10.1111/j.1365-246X.1976.tb01251.x. URL. http://onlinelibrary.wiley.com/doi/10.1111/j.1365-246X.1976.tb01251.x/abstract.

Peter, D., Komatitsch, D., Luo, Y., Martin, R., Le Goff, N., Casarotti, E., Le Loher, P., Magnoni, F., Liu, Q., Blitz, C., et al., 2011. Forward and adjoint simulations of seismic wave propagation on fully unstructured hexahedral meshes. Geophys. J. Int. 186 (2), 721–739.

Richardson, D.C., Bottke, W.F., Love, S.G., 1998. Tidal distortion and disruption of earth-crossing asteroids. Icarus 134, 47–76. http://dx.doi.org/10.1006/icar.1998.5954.

Richardson, D.C., Bottke, W.F., Love, S.G., 1998. Tidal distortion and disruption of earth-crossing asteroids. Icarus 134, 47–76. http://dx.doi.org/10.1006/icar.1998.5954.

Richardson, J.E., Melosh, H.J., Greenberg, R., 2004. Impact-induced seismic activity on Asteroid 433 Eros: a surface modification process. Science 306 (5701), 1526–1529. http://dx.doi.org/10.1126/science.1104731 arXiv: http://www.sciencemag.org/cgi/reprint/306/5701/1526.pdf http://www.sciencemag.org/cgi/content/abstract/306/5701/1526. URL.

Richardson Jr., J.E., Melosh, H.J., Greenberg, R.J., O'Brien, D.P., 2005. The global effects of impact-induced seismic activity on fractured asteroid surface morphology. Icarus 179 (2), 325–349. http://dx.doi.org/10.1016/j.icarus.2005.07.005. URL. http://www.sciencedirect.com/science/article/B6WGF-4H3BM2M-1/2/510504ea315e4d48c7f33abd0a93becd.

Riner, M.A., Robinson, M.S., Eckart, J.M., Desch, S.J., 2008. Global survey of color variations on 433 Eros: implications for regolith processes and asteroid environments. Icarus 198, 67–76. http://dx.doi.org/10.1016/j.icarus.2008.07.007.

Robert, O., Lognonne, P., Scheeres, D.J., Goujon, N., Le Feuvre, M., Izzet, A., Blitz, C., Bowman, L., 2010. Seismology on a small body: expected results for the BASiX Discovery Mission proposal. In: AGU Fall Meeting Abstracts.

Robinson, M.S., Thomas, P.C., Veverka, J., Murchie, S.L., Wilcox, B.B., 2002. The geology of 433 Eros. Meteorit. Planet. Sci. 37, 1651–1684.

Saito, J., Miyamoto, H., Nakamura, R., Ishiguro, M., Michikami, T., Nakamura, A.M., Demura, H., Sasaki, S., Hirata, N., Honda, C., Yamamoto, A., Yokota, Y., Fuse, T., Yoshida, F., Tholen, D.J., Gaskell, R.W., Hashimoto, T., Kubota, T., Higuchi, Y., Nakamura, T., Smith, P., Hiraoka, K., Honda, T., Kobayashi, S., Furuya, M., Matsumoto, N., Nemoto, E., Yukishita, A., Kitazato, K., Dermawan, B., Sogame, A., Terazono, J., Shinohara, C., Akiyama, H., 2006. Detailed images of Asteroid 25143 Itokawa from Hayabusa. Science 312 (5778), 1341–1344. http://dx.doi.org/10.1126/science.1125722 arXiv: http://www.sciencemag.org/cgi/reprint/312/5778/1341.pdf.

Scheeres, D.J., Britt, D., Carry, B., Holsapple, K.A., 2015. Asteroid Interiors and Morphology, pp. 745–766.

Scheirich, P., Pravec, P., 2009. Modeling of lightcurves of binary asteroids. Icarus 200, 531–547. http://dx.doi.org/10.1016/j.icarus.2008.12.001.

Scheirich, P., Pravec, P., Jacobson, S., Ďurech, J., Kušnirák, P., Hornoch, K., Mottola, S., Mommert, M., Hellmich, S., Pray, D., Polishook, D., Krugly, Y., Inasaridze, R., Kvaratskhelia, O., Ayvazian, V., Slyusarev, I., Pittichov, J., Jehin, E., Manfroid, J., Gillon, M., Galád, A., Pollock, J., Licandro, J., Alí-Lagoa, V., Brinsfield, J., Molotov, I., 2015. The binary near-earth asteroid (175706) 1996 {FG_3} an observational constraint on its orbital evolution. Icarus 245, 56–63. http://dx.doi.org/10.1016/j.icarus.2014.09.023. URL. http://www.sciencedirect.com/science/article/pii/S0019103514004850.

Schenk, P.M., Asphaug, E., McKinnon, W.B., Melosh, H.J., Weissman, P.R., 1996. Cometary nuclei and tidal disruption: the geologic record of Crater chains on Callisto and Ganymede. Icarus 121, 249–274. http://dx.doi.org/10.1006/icar.1996.0084.

Sens-Schönfelder, C., Larose, E., 2010. Lunar noise correlation, imaging and monitoring. Earthq. Sci. 23, 519–530. http://dx.doi.org/10.1007/s11589-010-0750-6.

Shearer, P.M., 2007. Seismic scattering in the deep earth. Precursors 10 (4), 695–730.

Sierks, H., Lamy, P., Barbieri, C., Koschny, D., Rickman, H., Rodrigo, R., A'Hearn, M.F., Angrilli, F., Barucci, M.A., Bertaux, J.-L., Bertini, I., Besse, S., Carry, B., Cremonese, G., Da Deppo, V., Davidsson, B., Debei, S., De Cecco, M., De Leon, J., Ferri, F., Fornasier, S., Fulle, M., Hviid, S.F., Gaskell, R.W., Groussin, O., Gutierrez, P., Ip, W., Jorda, L., Kaasalainen, M., Keller, H.U., Knollenberg, J., Kramm, R., Kührt, E., Küppers, M., Lara, L., Lazzarin, M., Leyrat, C., Moreno, J.J.L., Magrin, S., Marchi, S., Marzari, F., Massironi, M., Michalik, H., Moissl, R., Naletto, G., Preusker, F., Sabau, L., Sabolo, W., Scholten, F., Snodgrass, C., Thomas, N., Tubiana, C., Vernazza, P., Vincent, J.-B., Wenzel, K.-P., Andert, T., Pätzold, M., Weiss, B.P., 2011. Images of Asteroid 21 Lutetia: A remnant planetesimal from the early solar system. Science 334, 487. http://dx.doi.org/10.1126/science.1207325.

Takatsubo, J., Kishi, T., 1990. Quantitative acoustic emission source characterization of microcrackings in steel. Res. Nondestruct. Eval. 1, 219–233. http://dx.doi.org/10.1080/09349849009409478.

Taylor, P.A., Margot, J.-L., 2010. Tidal evolution of close binary asteroid systems. Celest. Mech. Dyn. Astronomy 108, 315–338. http://dx.doi.org/10.1007/s10569-010-9308-0. arXiv:1101.1500.

Teanby, N.A., Wookey, J., 2011. Seismic detection of meteorite impacts on Mars. Phys. Earth Planet. Interiors 186, 70–80. http://dx.doi.org/10.1016/j.pepi.2011.03.004.

Thomas, P.C., Robinson, M.S., 2005. Seismic resurfacing by a single impact on the asteroid 433 Eros. Nature 436, 366–369. http://dx.doi.org/10.1038/nature03855.

Thomas, P.C., Joseph, J., Carcich, B., Veverka, J., Clark, B.E., Bell, J.F., Byrd, A.W., Chomko, R., Robinson, M., Murchie, S., Prockter, L., Cheng, A., Izenberg, N., Malin, M., Chapman, C., McFadden, L.A., Kirk, R., Gaffey, M., Lucey, P.G., 2002. Eros: shape, topography, and slope processes. Icarus 155, 18–37. http://dx.doi.org/10.1006/icar.2001.6755.

Vasin, R.N., Nikitin, A.N., Lokajicek, T., Rudaev, V., 2006. Acoustic emission of quasi-isotropic rock samples initiated by temperature gradients. Izvestiya Phys. Solid Earth 42, 815–823. http://dx.doi.org/10.1134/S1069351306100053.

Veverka, J., Robinson, M., Thomas, P., Murchie, S., Bell, I., J. F, Izenberg, N., Chapman, C., Harch, A., Bell, M., Carcich, B., Cheng, A., Clark, B., Domingue, D., Dunham, D., Farquhar, R., Gaffey, M.J., Hawkins, E., Joseph, J., Kirk, R., Li, H., Lucey, P., Malin, M., Martin, P., McFadden, L., Merline, W.J., Miller, J.K., Owen, J., W. M, Peterson, C., Prockter, L., Warren, J., Wellnitz, D., Williams, B.G., Yeomans, D.K., 2000. NEAR at Eros: imaging and spectral results. Science 289 (5487), 2088–2097. http://dx.doi.org/10.1126/science.289.5487.2088 arXiv: http://www.sciencemag.org/cgi/reprint/289/5487/2088.pdf. http://www.sciencemag.org/cgi/content/abstract/289/5487/2088. URL.

Veverka, J., Thomas, P.C., Robinson, M., Murchie, S., Chapman, C., Bell, M., Harch, A., Merline, W.J., Bell, J.F., Bussey, B., Carcich, B., Cheng, A., Clark, B., Domingue, D., Dunham, D., Farquhar, R., Gaffey, M.J., Hawkins, E., Izenberg, N., Joseph, J., Kirk, R., Li, H., Lucey, P., Malin, M., McFadden, L., Miller, J.K., Owen, W.M., Peterson, C., Prockter, L., Warren, J., Wellnitz, D., Williams, B.G., Yeomans, D.K., 2001. Imaging of small-scale features on 433 Eros from NEAR: evidence for a complex regolith. Science 292, 484–488. http://dx.doi.org/10.1126/science.1058651.

Vincent, J.-B., Schenk, P., Nathues, A., Sierks, H., Hoffmann, M., Gaskell, R., Marchi, S., O'Brien, D., Sykes, M., Russell, C., Fulchignoni, M., Kellerg, H., Raymond, C., Palmer, E., Preusker, F., 2013. Crater depth-to-diameter distribution and surface properties of (4) vesta. Planet. Space Sci. http://dx.doi.org/10.1016/j.pss.2013.09.003. http://www.sciencedirect.com/science/article/pii/S0032063313002304. URL.

Vinnik, L., Chenet, H., Gagnepain-Beyneix, J., Lognonne, P., 2001. First seismic receiver functions on the moon. Geophys. Res. Lett. 28, 3031–3034. http://dx.doi.org/10.1029/2001GL012859.

Walker, J.D., Huebner, W.F., 2004. Loading sources for seismological investigations of near-Earth objects. Adv. Space Res. 33, 1564–1569. http://dx.doi.org/10.1016/S0273-1177(03)00454-X.

Walsh, K.J., Richardson, D.C., 2006. Binary near-Earth asteroid formation: Rubble pile model of tidal disruptions. Icarus 180 (1), 201–216. http://dx.doi.org/10.1016/j.icarus.2005.08.015. URL. http://www.sciencedirect.com/science/article/B6WGF-4HDX71W-2/2/df6330746c9a9d8d4ddeeacf2294a7c3.

Walsh, K.J., Richardson, D.C., Michel, P., 2008. Rotational breakup as the origin of small binary asteroids. Nature 454, 188–191. http://dx.doi.org/10.1038/nature07078.

Walter, W.R., Brune, J.N., 1993. Spectra of seismic radiation from a tensile crack. J. Geophys. Res. 98, 4449–4459. http://dx.doi.org/10.1029/92JB02414.

Watters, T.R., Thomas, P.C., Robinson, M.S., 2011. Thrust faults and the near-surface strength of asteroid 433 Eros. Geophys. Res. Lett. 38, 2202. http://dx.doi.org/10.1029/2010GL045302.

Williams, D.A., O'Brien, D.P., Schenk, P.M., Denevi, B.W., Carsenty, U., Marchi, S., Scully, J.E., Jaumann, R., Sanctis, M.C.D., Palomba, E., Ammannito, E., Longobardo, A., Magni, G., Frigeri, A., Russell, C.T., Raymond, C.A., Davison, T.M., 2013. Lobate and flow-like features on asteroid vesta. Planet. Space Sci. http://dx.doi.org/10.1016/j.pss.2013.06.017. URL. http://www.sciencedirect.com/science/article/pii/S003206331300158X.

Yasui, M., Matsumoto, E., Arakawa, M., 2015. Experimental study on impact-induced seismic wave propagation through granular materials. Icarus 260, 320–331. http://dx.doi.org/10.1016/j.icarus.2015.07.032.

Yingst, R., Mest, S., Berman, D., Garry, W., Williams, D., Buczkowski, D., Jaumann, R., Pieters, C., Sanctis, M.D., Frigeri, A., Corre, L.L., Preusker, F., Raymond, C., Reddy, V., Russell, C., Roatsch, T., Schenk, P., 2014. Geologic mapping of vesta. Planet. Space Sci. http://dx.doi.org/10.1016/j.pss.2013.12.014. URL. http://www.sciencedirect.com/science/article/pii/S0032063313003486.

Yong, C., Wang, C.-y., 1980. Thermally induced acoustic emission in westerly granite. Geophys. Res. Lett. 7, 1089–1092. http://dx.doi.org/10.1029/GL007i012p01089.

Zuber, M.T., Smith, D.E., Cheng, A.F., Garvin, J.B., Aharonson, O., Cole, T.D., Dunn, P.J., Guo, Y., Lemoine, F.G., Neumann, G.A., Rowlands, D.D., Torrence, M.H., 2000. The shape of 433 Eros from the NEAR-shoemaker laser rangefinder. Science 289 (5487), 2097–2101. http://dx.doi.org/10.1126/science.289.5487.2097 arXiv:http://www.sciencemag.org/content/289/5487/2097.full.pdf. http://www.sciencemag.org/content/289/5487/2097.abstract. URL.